České vysoké učení technické v Praze
Fakulta jaderná a fyzikálně inženýrská

Katedra fyziky
Obor: Jaderná a částicová fyzika

Globální polarizace lambda hyperonu v jádro-jaderných srážkách na experimentu STAR

VÝZKUMNÝ ÚKOL

Vypracoval: Bc. Ondřej Lomický
Vedoucí práce: Dr. Barbara Trzeciak, Ph.D.
Rok: 2021

Czech Technical University in Prague
Faculty of Nuclear Sciences and Physical Engineering

Department of Physics
Study program: Nuclear and Particle Physics

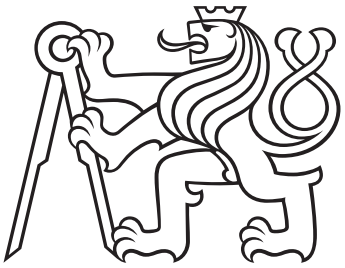

Global polarization of lambda hyperons in heavy-ion collisions at STAR

RESEARCH TASK

Author: Bc. Ondřej Lomický
Supervisor: Dr. Barbara Trzeciak, Ph.D.
Year: 2021

ČESKÉ VYSOKÉ UČENÍ TECHNICKÉ V PRAZE
FAKULTA JADERNÁ A FYZIKÁLNĚ INŽENÝRSKÁ
PRAHA 1 - STARÉ MĚSTO, BŘEHOVÁ 7 - PSČ 115 19

Katedra: fyziky **Akademický rok:** 2020/2021

VÝZKUMNÝ ÚKOL

Student: Bc. Ondřej Lomický

Studijní program: Jaderná a částicová fyzika

Vedoucí úkolu: Dr. Barbara Antonina Trzeciak, Ph.D.

Konzultant - doc. Mgr. Jaroslav Bielčík, Ph.D.

Název úkolu (česky/anglicky):
Globální polarizace lambda hyperonu v jádro-jaderných srážkách na experimentu STAR/
Global polarization of lambda hyperons in heavy-ion collisions at STAR

Pokyny pro vypracování:

1) Současné výsledky globální polarizace lambda hyperonu v jádro-jaderných srážkách
2) Experiment STAR
3) Rekonstrukce roviny události prvního řádu
4) Rekonstrukce lambda hyperonu a úhlová distribuce dceřiných protonů
5) Diskuze a závěr

Součástí zadání výzkumného úkolu je jeho uložení na webové stránky katedry fyziky. Výzkumný úkol bude vypracován v anglickém jazyce.

Literatura:

[1] H. Satz: Extreme States of Matter in Strong Interaction Physics, Lecture Notes in Physics 945, Springer, 2018
[2] C. Pruneau: Data Analysis Techniques for Nuclear and Particle Physics, CRC Press, 2016
[3] I. Upsal: Global Polarization of the Lambda system in the STAR BES, Ph.D. Thesis, The Ohio State University, 2018
[4] J. Adam, et. al.: Global polarization of Lambda hyperons in Au+Au collisions at 200 GeV, Phys. Rev. C 98, 014910 (2018)

Datum zadání: 23. 10. 2020 .....

Datum odevzdání: 30. 06. 2021 ***vedoucí katedry***

Prohlášení

Prohlašuji, že jsem svou výzkumnou práci vypracoval samostatně a použil jsem pouze podklady (literaturu, projekty, SW atd.) uvedené v přiloženém seznamu.

Nemám závažný důvod proti použití tohoto školního díla ve smyslu § 60 Zákona č. 121/2000 Sb., o právu autorském, o právech souvisejících s právem autorským a o změně některých zákonů (autorský zákon).

V Praze dne ....

Bc. Ondřej Lomický

Poděkování

Chtěl bych moc poděkovat vedoucí své práce Dr. Barbaře Trzeciak, Ph.D. za velkou trpělivost, pomoc a podmětné rady během vypracovávání této práce. Dále děkuji též doc. Mgr. Jaroslavu Bielčíkovi, Ph.D. za pomoc při snaze pochopit teoretickou rovinu této práce.

Bc. Ondřej Lomický

Název práce:

Globální polarizace lambda hyperonu v jádro-jaderných srážkách na experimentu STAR

Autor: Bc. Ondřej Lomický

Studijní program: Jaderná a částicová fyzika
Druh práce: Výzkumný úkol

Vedoucí práce: Dr. Barbara Trzeciak, Ph.D.
Katedra fyziky, Fakulta jaderná a fyzikálně inženýrská, České vysoké učení technické v Praze
Konzultant: doc. Mgr. Jaroslav Bielčík, Ph.D.
Katedra fyziky, Fakulta jaderná a fyzikálně inženýrská, České vysoké učení technické v Praze

Abstrakt: Kvark-gluonové plazma, nové, horké a husté skupenství hmoty, lze vytvořit v relativistických srážkách těžkých jader. Studiem jeho vlastností se zabývá například Brookhavenská národní laboratoř. Ukázalo se, že tato horká jaderná hmota se svými vlastnostmi blíží dokonalé kapalině a že může dosahovat nejvyšší hodnoty vířivosti, která kdy byla pozorována. Právě takto vysoká výřivost ovlivňuje spin vyprodukovaných částic, jehož orientace může být určena pomocí Λ hyperonů. Tato práce diskutuje kroky nutné k identifikaci Λ hyperonu a především určení orientace jeho spinu. Cílem analýzy bylo získat globální polarizaci lambda hyperonu ze srážek Au-Au s energií 27 GeV v těžišťové soustavě na detektoru STAR.
Klíčová slova: STAR, lambda, polarizace, rovina události

Title:

Global polarization of lambda hyperons in heavy-ion collisions at STAR

Author: Bc. Ondřej Lomický

Abstract: Quark-gluon plasma, a new hot and dense state of matter, can be created in relativistic heavy-ion collisions. Brookhaven National Laboratory is an example of a place where its properties are studied. It was shown that this hot nuclear matter is almost a perfect fluid and that it can reach the highest value of vorticity which have been ever observed. Such high vorticity influences the orientation of the produced particle spin. The orientation can be reconstructed via Λ hyperons. This thesis discusses the steps needed for the identification of the Λ hyperon, especially the determination of its spin orientation. The goal of this analysis was to reconstruct the global polarization of Λ hyperon using the data from Au-Au collisions at center-of-mass energy 27 GeV from the STAR experiment.
Key words: STAR, lambda, polarization, event plane

Contents

Introduction

Quark-Gluon Plasma (QGP) is a novel state of matter, where quarks and gluons are asymptotically free. The QGP is believed to exist in the beginning of the Universe shortly after the Big Bang. In a laboratory, the QGP can be studied in relativistic heavy-ion collisions. However, the lifetime of this matter in heavy-ion collisions is very short (few units of fm/c [1]), therefore the direct measurement of its properties is impossible. The QGP properties can be studied using various probes, such as: soft probes (i.e. particles with transverse momenta $p_{\mathrm{T}} < 2$ GeV/c), hard probes (i.e. particles with $p_{\mathrm{T}} > 10$ GeV/c) or electromagnetic probes (i.e. photons and dileptons) [2], [3]. For example, studies of the medium fluid dynamical expansion has revealed that the QGP is almost perfect liquid [4], [5]. More precisely the ratio of shear viscosity to entropy is close to the lowest value determined from the quantum mechanics [6].

Other properties of the QGP medium are also extensively studied. For example, the QGP's vorticity is estimated as the highest being ever observed in the universe [7]. The vorticity describes rotation of the system having the same direction as the system angular momentum and it is a thermodynamic quantity needed for description of the local fluid [8]. The initial vorticity can be studied indirectly via measurements of particle polarization (spin alignment). The spin-orbital coupling can cause the preferential orientation of particle spins along the direction of the system angular momentum. Therefore, the measured value is align between the global angular momentum of a non-central collision and the spin of the emitted particles.

This work is focused on steps needed to compute the global polarization. The natural choice of the particle is in this case the lightest strange baryons produced in high abundances, Λ or $\overline{\Lambda}$, because of its self-analyzing nature of decay. More precisely, the direction of the emitted proton from the parity-violating weak decays of Λ is highly correlated with the Λ spin.

The Λ particle can be reconstructed via its decay products (daughters), i. e. protons and pions. This task can be performed via Kalman Filter [9]. The second part of the polarization analysis is reconstruction of the daughter proton angular distribution in the Λ rest frame. One has to first estimate the reaction plane which is related to the geometry of a collision, using an event plane detector. The other important ingredient related to the reaction plane is its resolution which has to be also estimated. Furthermore, there are different analysis techniques that allow to measure the polarization, e.g. an invariant mass or event plane method that are presented in this work. The comparison between them can help to estimate the precision of the

results [10].

Data analyzed in this task are from Au-Au collisions at $\sqrt{s_{\mathrm{NN}}} = 27$ GeV collected in 2018 by the STAR experiment at RHIC.

The measured Λ and $\overline{\Lambda}$ polarization when compared to different model predictions may reveal information about the vorticity of the QGP medium. This value is important for the QGP model because the vorticity as the thermodynamic quantity can probe the QGP formation and its dynamics.

Chapter 1

Global lambda polarization in heavy-ion collisions

In this chapter, the basic information about the Quark-Gluon Plasma and its properties will be introduced. Next, the concept of the QGP vorticity and its relation to the global hyperon polarization is discussed.

1.1 Quark-gluon plasma

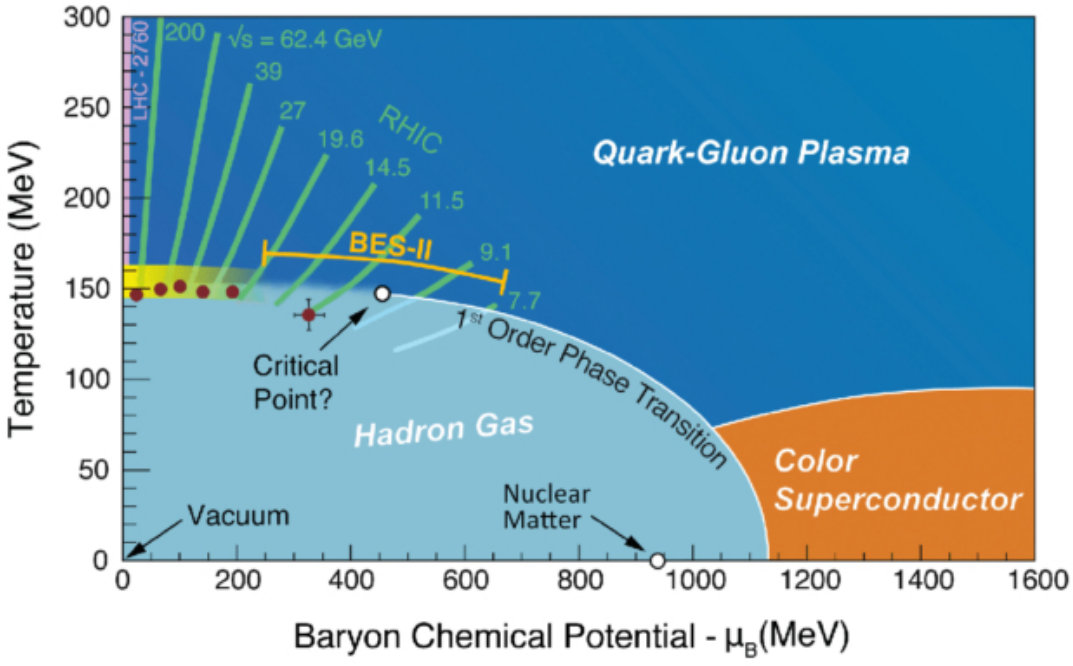

Figure 1.1: The QCD phase diagram as function of temperature and baryon chemical potential μ_B [11].

The Quark-Gluon Plasma (QGP) is a novel state of matter where quarks and

gluons are liberated. The first measured evidence of the QGP occurred at CERN in 2000 [12] and the existence of the QGP was later confirmed by RHIC at BNL [13], [14]. The existence of this state was already predicted by the Standard Model of strong interaction. In particular, this model described the state of matter in which partons (quarks and gluons forming hadrons) are asymptotically free. The phase transition from hadron gas (classical matter) to QGP is expected to occur at temperature $T = (156.5 \pm 1.5)$ MeV [15] from the lattice QCD calculations at $\mu_B = 0$. One can imagine this process as melting of hadrons [16]. This phase transition is depicted in the QCD phase diagram in Fig. 1.1. It is excepted that the QGP was presented in the early Universe (10^{-5} s after the Big Bang) or can be found in the center of compact stars (white dwarfs, neutron stars and quark stars) [17]. Both of these places are currently unattainable for us. Other possibility how to create QGP is in a laboratory via high-energy nucleus-nucleus collision because the energy density in the colliding heavy nuclei going through each other is high enough.

Unfortunately, the lifetime of the QGP which is created in a last manner is pretty short (up to 10-15 fm/c) [18]. Therefore, its properties (e.g. temperature, pressure, energy density, entropy, baryon chemical potential) cannot be measured directly but via different experimental probes. Results are then compared to theoretical predictions, e.g. statistical model [19]. The space-time evolution of the QGP including all stages, such as pre-equilibrium, QGP, mixed phase of the QGP and hadron gas, and hadron gas is depicted in Fig. 1.2.

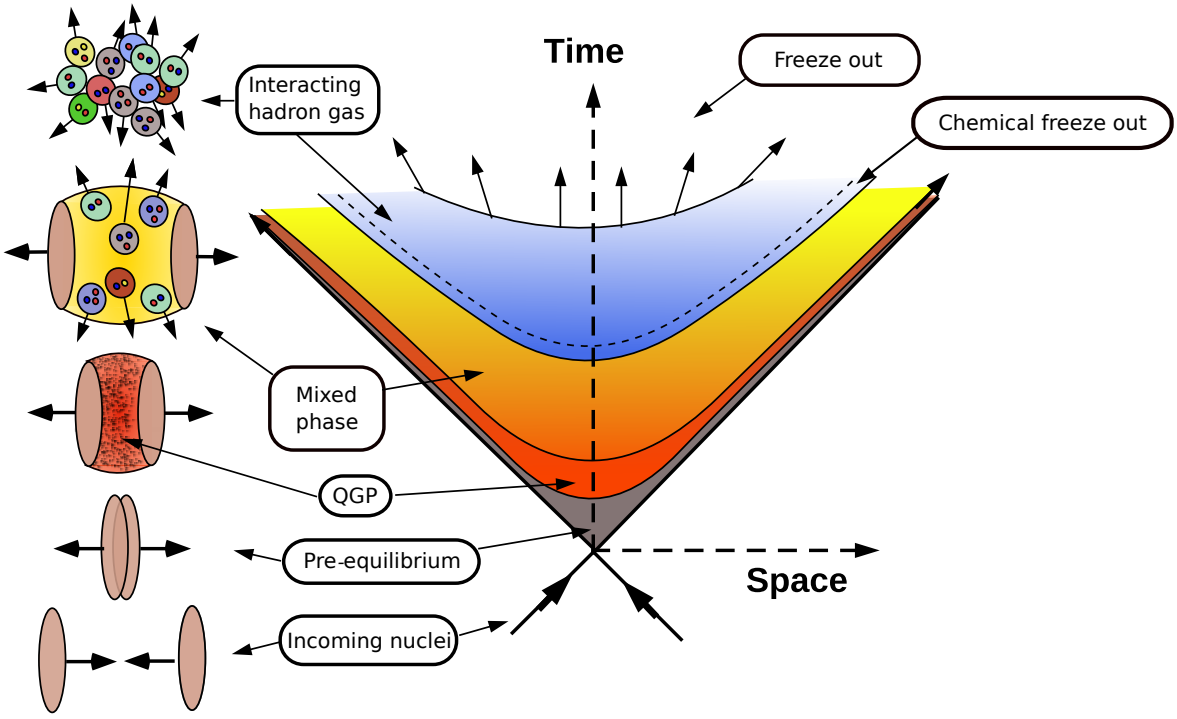

Figure 1.2: Space-time diagram of a heavy-ion collision including various stage of the evolution of the medium [21], modified.

Heavy-ion (HI) collisions data together with related hydrodynamics theories show

that the QGP can be described as a nearly perfect liquid. By the word nearly is meant that the liquid has low ratio of shear viscosity to entropy density ($\eta/s \approx 0.12$) [20].

One of the observables that can be used to study presence of the QGP in HI collisions is the nuclear modification factor R_{AA}. It is defined as a normalized ratio between the numbers of produced particles in HI and p-p collision as a function of transverse momentum p_{T}, i.e.

$$R_{\mathrm{AA}}(p_{\mathrm{T}}) = \frac{1}{\langle N_{coll} \rangle} \frac{\frac{\mathrm{d}N_{\mathrm{AA}}}{\mathrm{d}p_{\mathrm{T}}}(p_{\mathrm{T}})}{\frac{\mathrm{d}N_{\mathrm{pp}}}{\mathrm{d}p_{\mathrm{T}}}(p_{\mathrm{T}})} \tag{1.1}$$

where $\langle N_{coll} \rangle$ is number of binary nucleon-nucleon collisions. One expects that R_{AA} equals one in the case of the absence of the QGP and other nuclear effects [22].

The next observable is azimuthal anisotropy of produced particles. The azimuthal particle distribution can be written as a Fourier series w.r.t. the reaction plane as follows

$$E\frac{\mathrm{d}^3N}{\mathrm{d}p^3} = \frac{1}{2\pi}\frac{\mathrm{d}^2N}{p_{\mathrm{T}}\mathrm{d}p_{\mathrm{T}}\mathrm{d}y}\left\{1 + \sum_{n=1}^{\infty} 2v_n \cos[n(\phi - \Psi_{\mathrm{RP}})]\right\} \tag{1.2}$$

where ϕ is the azimuthal angle of measured particle, Ψ_{RP} is the reaction plane angle and v_n is the n-th flow coefficient. In particular, the v_2 (so-called elliptic flow) can indicate the creation of the deconfined medium [23].

1.2 Vorticity of the QGP

The vorticity $\vec{\omega}$ is a pseudovector field describing rotation at a point in a fluid. It is defined as

$$\vec{\omega} = \vec{\nabla} \times \vec{v} \tag{1.3}$$

where $\vec{\nabla} = (\frac{\partial}{\partial x}; \frac{\partial}{\partial y}; \frac{\partial}{\partial z})$ and $\vec{v}$ is a velocity at the point[1]. The units of ω are inverse time s^{-1}. The vorticity is twice larger than the angular momentum at the chosen point. The direction of the vorticity is given by the right-hand rule, i.e. if your curled fingers on the right hand show the direction of the rotation, the raised thumb shows the direction of $\vec{\omega}$ [24].

Fig. 1.3 illustrates the related $\vec{v}$ vectors (yellow arrows) and the final direction of the rotation of the emerging QGP in non-central HI collisions with an impact parameter $\vec{b}$. The upper figure shows a situation before the collision. The lower figure presents a situation after the collision where the participants of the collision are "melted" and the spectators continue ahead being deflected from the z-axis by repulse impulse. The depicted deflection corresponds to positive directed flow v_1 in the forward direction [8]. Actually, the deflection is also possible to opposite angle with respect to the z-axis. This can occur in the case that the collision energy is much lower and the attractive forces are more significant.

[1]Sometimes the vorticity is defined as $\vec{\omega} = \frac{1}{2}\vec{\nabla} \times \vec{v}$. Then the angular momentum at the point has the same value [7].

The depicted deflection of the spectators is very important to understand the vorticity of the QGP. One has to know the direction of the angular momentum which gives the average direction of the system vorticity. The forward detectors at large pseudorapidity, measuring the spectators, can be used to estimate the angular momentum of the system $\hat{J}_{\text{sys}}$ by means of the so-called event plane [8]. This will be discussed more in detail in Chapter 4.1.

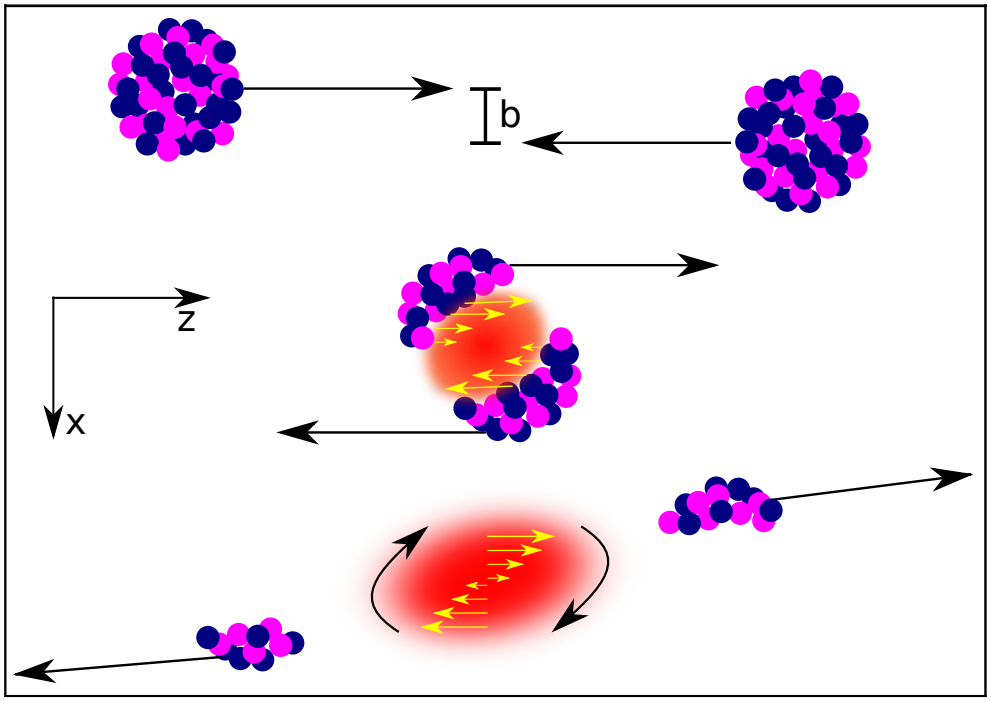

Figure 1.3: Schematic of HI collision with impact parameter b in the xz-plane where z is the beam direction.

The vorticity of the QGP was estimated to be $\omega \approx (9 \pm 1) \times 10^{21}$ s^{-1} [7] which shows that the QGP can be perceived as the perfect vortical fluid. For comparison, one can introduce vorticity of different fluids:

- Solar subsurface flow - $\omega \approx 10^{-7}$ s^{-1}
- Terrestrial atmospheric patterns - $\omega \approx 10^{-7} - 10^{-5}$ s^{-1}
- Supercell tornado cores - $\omega \approx 10^{-1}$ s^{-1}
- The Great Red Spot of Jupiter - $\omega \approx 10^{-1}$ s^{-1}
- Heated soap bubbles - $\omega \approx 10^{-1}$ s^{-1}
- Turbulent flow in bulk superfluid He-II - $\omega \approx 10$ s^{-1}
- Superfluid nanodroplets - $\omega \approx 10^{7}$ s^{-1}

Hence, one can see that the QGP may be the most vortical fluid which has been ever observed in the universe.

1.3 Polarization of Lambda hyperon

The angular momentum of the created medium $\hat{J}_{sys}$ influences the spin of produced particles which can be then aligned along the direction of $\hat{J}_{sys}$ via spin-orbit coupling. This global polarization of the particles can be experimentally measured using hyperons (containing s-quark). Hyperons decay via weak decays whose property is that the decay (daughter) particles prefer the production in the spin direction of the mother hyperon. In the case of the antiparticles, the direction of daughter baryons is opposite to the mother hyperon spin direction. This process is depicted in Fig. 1.4, where $\vec{P}_\Lambda$ is the hyperon polarization and $\vec{p}_p^*$ with θ^* are the momentum of the daughter baryon and the angle between the polarization $\vec{P}_\Lambda$ and momentum $\vec{p}_p^*$ in the rest frame of the hyperon, respectively [10].

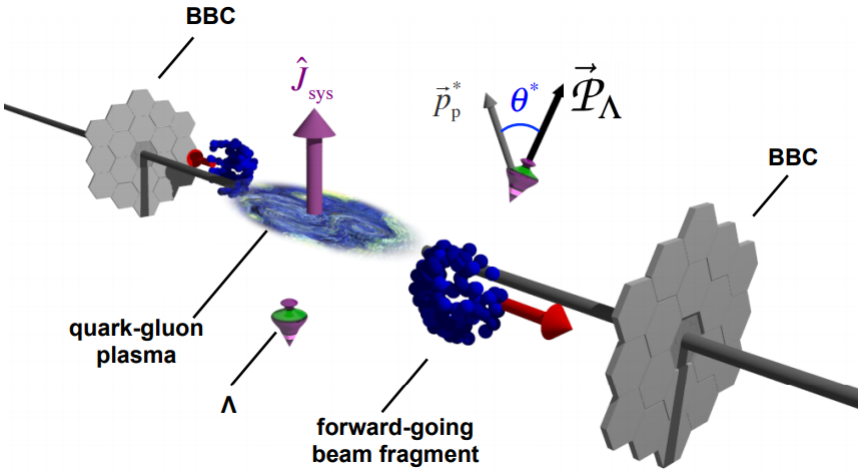

Figure 1.4: Schematic of a HI collision where the produced Λ (spinning tops) are polarized w.r.t. the angular momentum of the system $\hat{J}_{sys}$ [7].

The angular distribution of the daughter baryon can be expressed as

$$\frac{\mathrm{d}N}{\mathrm{d}\cos\theta^*} \propto 1 + \alpha_H P_H \cos\theta^* \tag{1.4}$$

where P_H is the polarization of the hyperon and α_H is its decay constant $\alpha_\Lambda = 0.732 \pm 0.014$ and $\alpha_{\overline{\Lambda}} = -0.758 \pm 0.010$ for Λ and $\overline{\Lambda}$, respectively [25]. Hence the global polarization can be measured via the daughter baryon distribution. Taking into account the resolution of the reconstructed event plane $\mathscr{R}_1$ the expression for the global angular polarization is

$$P_H = \frac{8}{\pi\alpha_H}\frac{\langle\sin\left(\Psi_1 - \phi_p^*\right)\rangle}{\mathscr{R}_1} \tag{1.5}$$

where Ψ_1 is the event plane of the first order, $\mathscr{R}_1$ is its resolution and ϕ_p^* is azimuthal angle of the daughter particle in the rest frame of mother hyperon. Due to their abundant production, often chosen hyperons for this measurement are Λ and $\overline{\Lambda}$ particles [7].

The measured global Λ and $\overline{\Lambda}$ polarization as a function of the collision energy is shown in Fig. 1.5. The most recent results from the ALICE experiment for energies $\sqrt{s_{\rm NN}} = 2.76$ TeV and 5.02 TeV are compared with the older ones from the STAR experiment at energies $\sqrt{s_{\rm NN}} = 7.7 - 62.4$ GeV and $\sqrt{s_{\rm NN}} = 200$ GeV. At 200 GeV where the measurement is so far the most precise, the obtained polarization of Λ and $\overline{\Lambda}$ hyperons is $\langle P_\Lambda \rangle = 0.277 \pm 0.040$ (stat.) $\pm \frac{0.039}{0.049}$ (syst.) % and $\langle P_{\overline{\Lambda}} \rangle = 0.240 \pm 0.045$ (stat.) $\pm \frac{0.039}{0.049}$ (syst.) % [10]. Moreover, one can measure global polarization of Ξ or Ω hyperons. Results from the STAR experiment in Au-Au collisions at $\sqrt{s_{\rm NN}} = 200$ GeV are also presented in Fig. 1.5 and compared to the Λ polarization measurements. The measured values are $\langle P_\Xi \rangle = 0.47 \pm 0.10$ (stat.) $\pm$ 0.23 (syst.) % for Ξ particles and $\langle P_\Omega \rangle = 1.11 \pm 0.87$ (stat.) $\pm$ 1.97 (syst.) % for Ω particles and are consistent with Λ hyperon polarization [26].

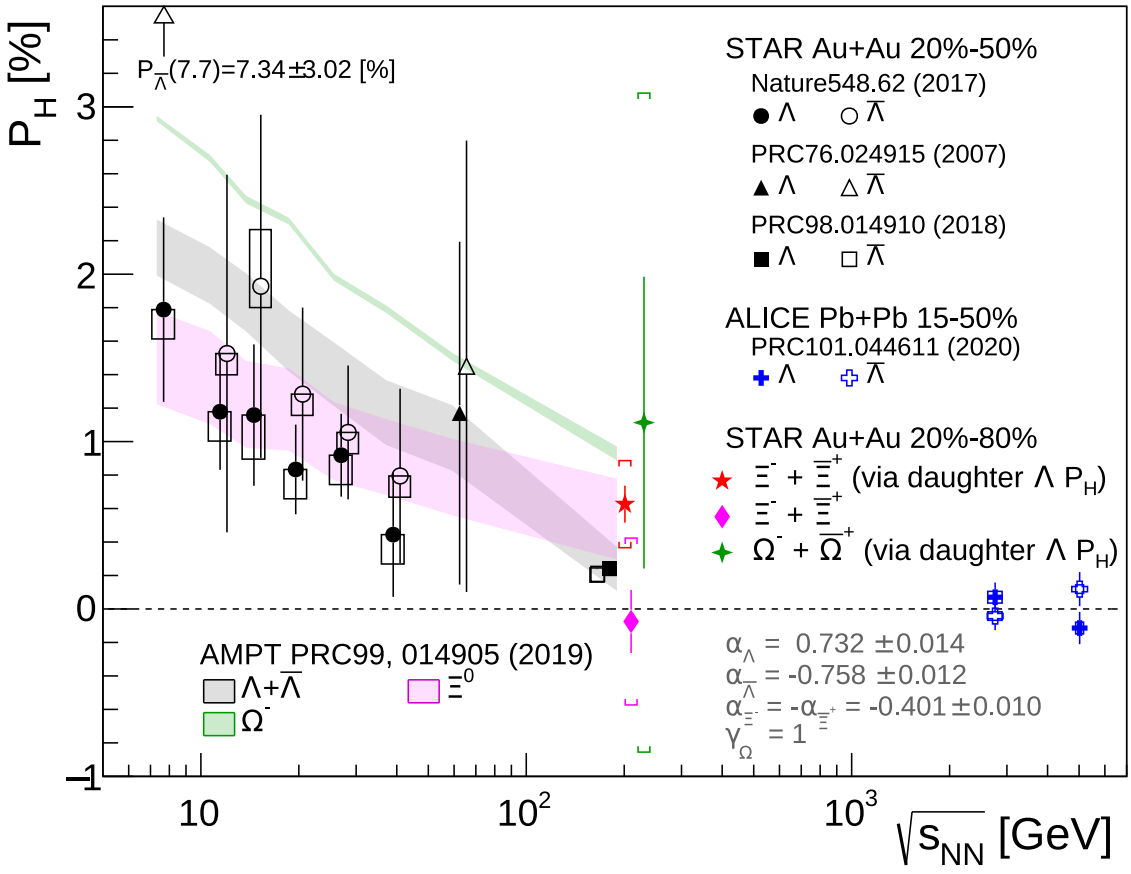

Figure 1.5: The global hyperon polarization $P_{\rm H}$ as a function of collision $\sqrt{s_{\rm NN}}$ for Λ, $\overline{\Lambda}$, Ξ and Ω particles [26].

In general, a decreasing trend of polarization with increasing energy of the collision can be seen. The energy dependence of the Λ polarization can be described, for example, by a multi-phase transport model (AMPT) [10]. These calculations also predict that lighter particles having higher spin may be more polarized by the system vorticity. The higher polarization for Ξ and Ω (multi-strange particles) could be caused by their earlier time of freeze-out. The feed-down effect (contribution of non-primary hyperons) reduces the measured polarization. This effect is more significant

for Λ hyperons than Ξ and Ω hyperons [10].

The dependence of the global hyperon polarization on centrality of collision can be seen in Fig. 1.6. The hyperon polarization is larger in the peripheral collisions indicating the centrality dependence of the fluid vorticity [10].

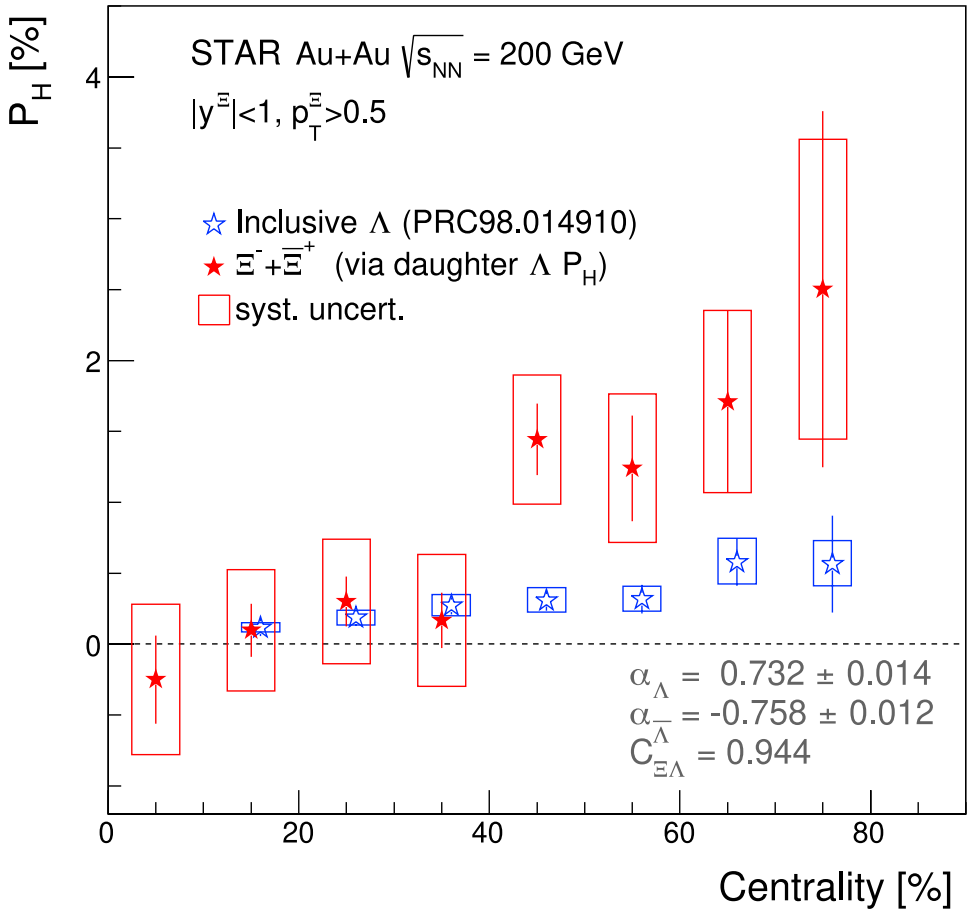

Figure 1.6: The global hyperon polarization $P_{\rm H}$ as a function of collision centrality for Λ and Ξ particles in Au-Au collisions at $\sqrt{s_{\rm NN}} = 200$ GeV [26].

Chapter 2

STAR experiment

In this chapter, the RHIC collider at BNL, the STAR experiment and the future plans of the RHIC transition to a new EIC collider are described.

2.1 RHIC

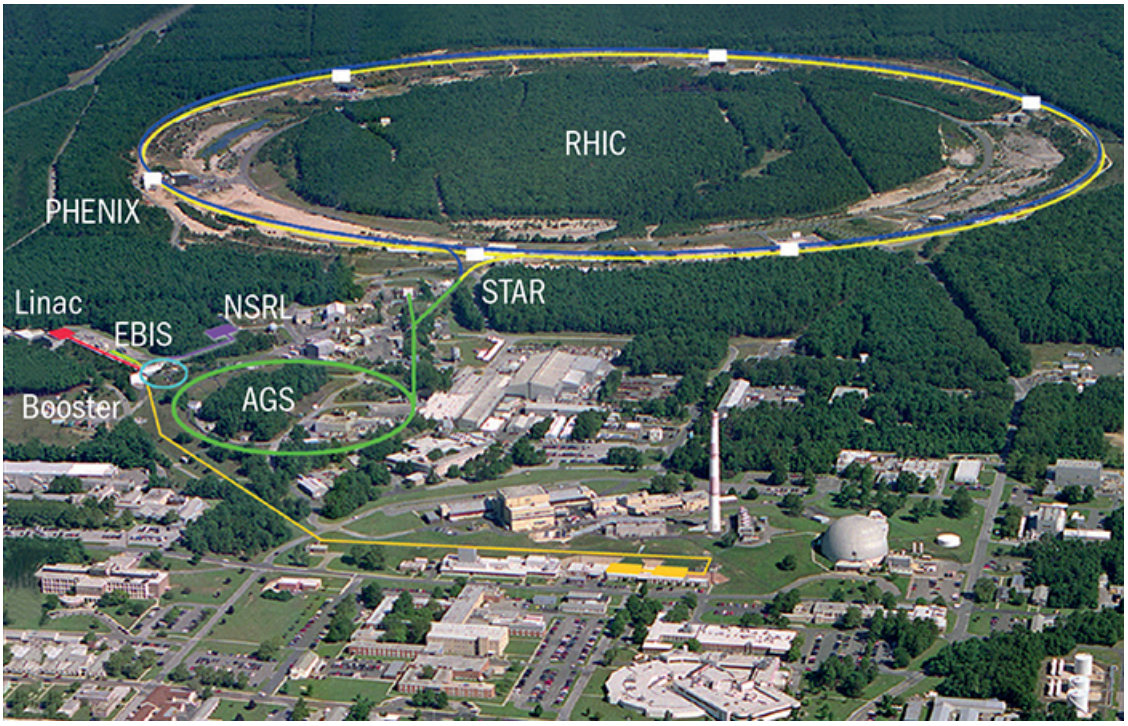

Figure 2.1: A photo of the RHIC accelerators with positions of STAR and PHENIX experiments indicated [27].

The Relativistic Heavy Ion Collider (RHIC) is a device at Brookhaven National Laboratory (BNL) on Long Island in the USA. The beginning of this collider was in the year 1983 during the Aurora meeting when was raised a task to prepare

parameters of the future collider. The building started from tunnels (the ring shape of approximately 3.8 km circumstance [28]) from the previous project Colliding Beam Accelerator (CBA), formerly ISABELLE [29]. One of the first main goals of the RHIC was to achieve low net baryon density in the central rapidity region [30]. The scheme of the RHIC can be seen in Fig. 2.1.

RHIC consists of two storage rings (yellow and blue) which cross at 6 interaction points (IPs) [31]. In 2000 at RHIC, there were four experiments running: STAR (6 o'clock position) that is still collecting data, PHENIX (8 o'clock position) that finished operations in 2016, and two smaller detectors BRAHMS (2 o'clock position) and PHOBOS (10 o'clock position) which were stopped in 2005. Currently, a new detector sPHENIX is being built [32].

The RHIC can collide protons, heavy ions such as Au, Cu or U nuclei or unequal species like p-Au, d-Au or ^{3}He-Au. Furthermore, the proton beam can be polarized [33], [34]. The center-of-mass (CMS) energies that can be reached by RHIC are between 7.7 GeV and 200 GeV per nucleon for Au-Au collisions and up to 510 GeV in the case of polarized protons. Overview of different species collided at different CMS energies at RHIC until 2020 can be seen in Fig. 2.2.

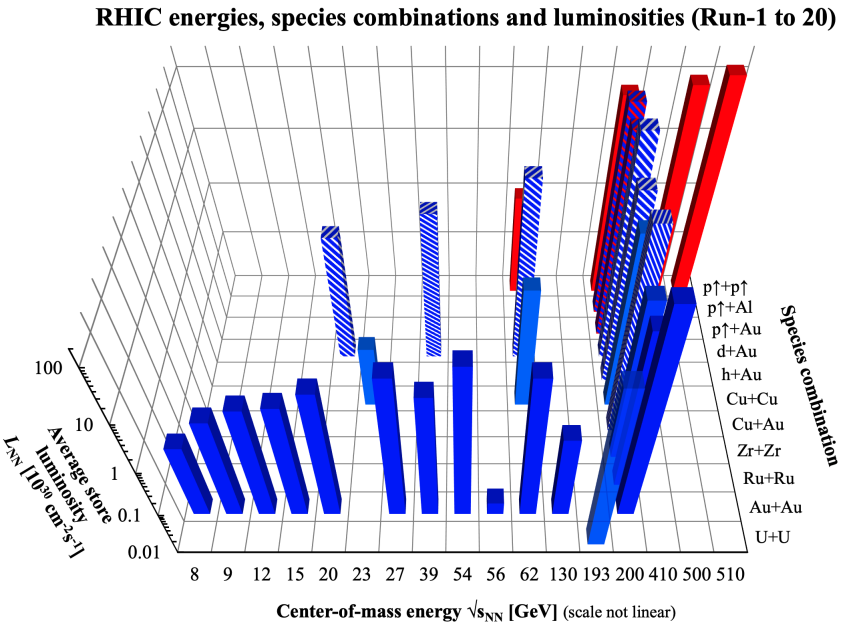

Figure 2.2: A graph of collided species combination, CMS energies and luminosities since 2000 [35].

2.2 STAR

The STAR experiment (Solenoidal Tracker At RHIC) was designed to measure and investigate the properties of strongly interacting matter (QGP) [36]. Before the upgrades of the STAR which were related to the Beam Energy Scan II (BES-II)

[37] scheduled from 2019 to 2020, the STAR detector consisted of 18 subsystem, examples of them can be seen in Fig. 2.3.

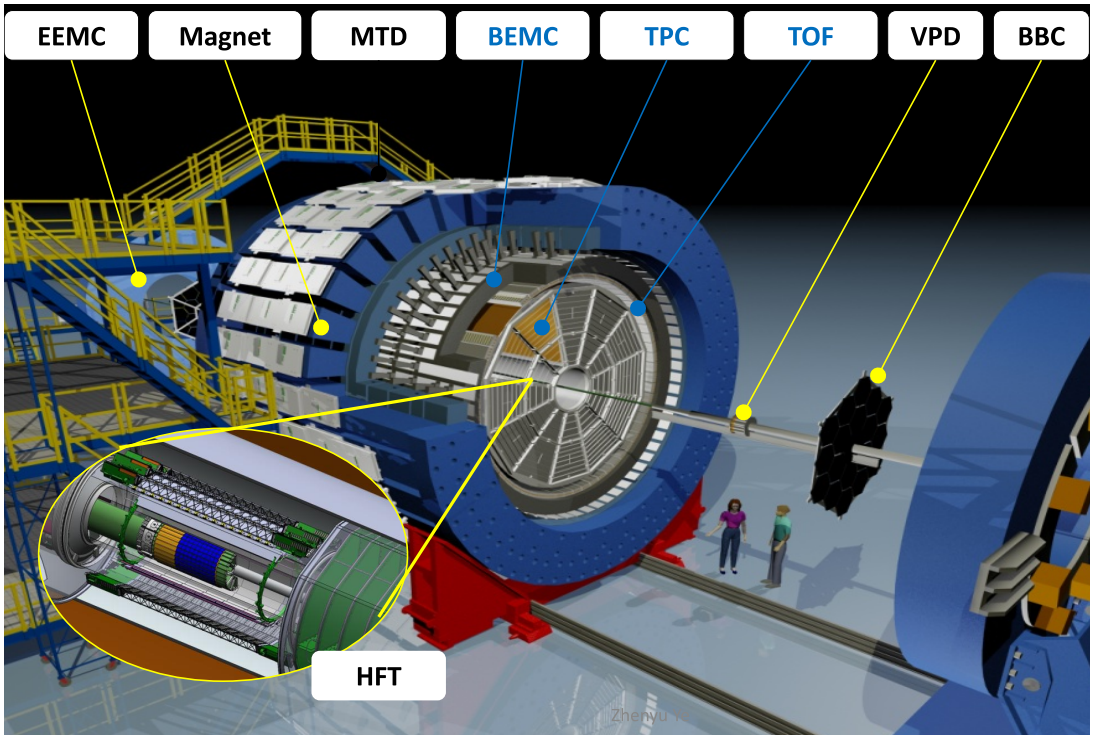

Figure 2.3: The layout of the STAR detector before the upgrade [42].

The Time Projection Chamber (TPC) [43] in the center of the STAR detector reconstructs tracks, measures momenta and identifies species of produced particles. The Particle IDentification (PID) is performed using information about particle ionization energy loss ($\mathrm{d}E/\mathrm{d}x$) in the TPC gas. The length of the TPC is 4.2 m and the outer diameter of the drift volume is 4 m. It covers approximately $|\eta| < 1.8$ units of pseudorapidity [43].

The Time of Flight (TOF) [44] detector is based on Multi-gap Resistive Plate Chamber (MRPC) technology and it was installed in 2003. The TOF has a time resolution $\lesssim$ 100 ps. It covers $-1 \leq \eta \leq 1$ units of rapidity. The TPC and TOF detectors are used together to separate some particle species. For instance, TPC alone can not separate pions and protons for transverse momenta $2.0 \lesssim p_T \lesssim 4.0$ GeV and TOF has an overall problem with the separation of pions and proton [44], [45].

The Barrel Electromagnetic Calorimeter (BEMC) [46] covers the TOF and TPC detector and its acceptance is $|\eta| < 1.0$ in full azimuthal angle. The BEMC consists of 120 calorimeter modules which are used for electromagnetic energy measurement. It is also used to identify electrons and it can trigger on high-p_{T} particles (e.g. jets, leading hadrons, direct photons, and electrons) [46].

The solenoidal magnet with uniform magnetic field is located along the beam direction. The strength of the magnetic field is 0.5 T [47]. The detectors TPC, TOF

and BEMC are placed inside of the magnet.

The Beam-Beam Counter (BBC) [48] is composed of scintillators located around the beam pipe on the east and west pole tips of the magnet. Both parts (annuli) of BBC are 3.75 m from the center of the STAR detector. The BBC covers range $3.4 < |\eta| < 5.0$ in full azimuthal range and it provides also a trigger for the polarized proton measurements [48].

The Vertex Position Detector (VPD) [49] or currently pseudo Vertex Position Detector (pVPD) integrated into the STAR trigger system provides the location of the collision vertex. It consists of two detectors on the west and east side of the STAR detector. Each of these parts is located immediately outside the beam pipe. The data from pVPD are the input to the minimum-bias trigger for Au-Au collisions [49], [50].

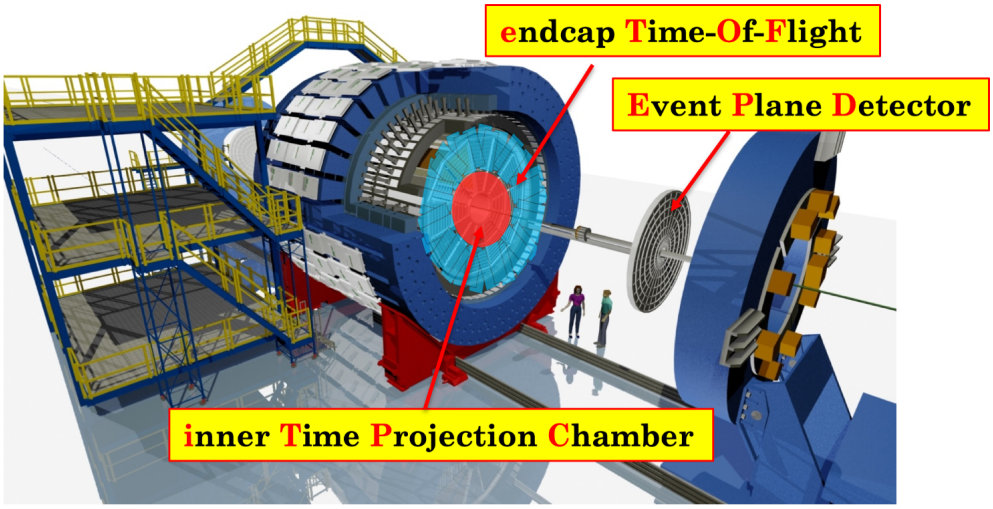

Figure 2.4: The layout of the STAR detector with highlighted upgraded parts such as iTPC, EPD and eTOF [51].

The main goals of BES-I program were exploration of the QGP phase diagram, search for the possible critical point of the QCD, and study of phase transition between hadronic and partonic matter [52]. The program was focused on collisions energies between 7.7 GeV and 19.6 GeV. However, the precision of some measurements (e.g. the net proton kurtosis, the directed flow, and the dilepton production [51]) was insufficient to draw precise physics conclusions. Therefore, before the next stage of BES (BES-II) the STAR detector underwent a couple of upgrades, namely the following detectors were installed: inner Time Projection Chamber (iTPC), Event Plane Detector (EPD), and endcap Time of flight detector (eTOF), as can be seen in Fig. 2.4 [51].

The almost final data acquired in BES II program (2020) are gathered in Tab. 2.1. As can be seen, the BES-II program has been very successful. Currently, the highest priorities are to complete the second phase of BES-II and start with Cold QCD forward physics program. The next plan is an exploration of the microstructure of the QGP via soft and hard probes in 2023-25 [53].

The fixed-target mode (FXT) at STAR extends the collision energy to lower values (namely 4.59, 7.3, and 31.2 GeV/nucleon in 2019 [38] and 3.85, 5.75, 9.8, 13.5, 19.5, 44.5, 70 and 100 GeV/nucleon in 2020 and 2021 [39], [40]) and is a part of the BES II. The position of the fixed target is 2.05 m west of the center of the STAR detector. Thin gold foil (1 mm) is used as the target. Few days of running (1-2 days) at each collision energy provides the sufficient statistics for BES II program [41].

Beam Energy (GeV/nucleon)	$\sqrt{s_{\mathrm{NN}}}$ (GeV)	μ_{B} (MeV)	Run Time	Number Events Requested (Recorded)	Date Collected
13.5	27	156	24 days	(560 M)	Run-18
9.8	19.6	206	36 days	400 M (582 M)	Run-19
7.3	14.6	262	60 days	300 M (324 M)	Run-19
5.75	11.5	316	54 days	230 M (235 M)	Run-20
4.59	9.2	373	in progress	160 M	Run20+20b
31.2	7.7 (FXT)	420	0.5+1.1 days	100 M (50 M+112 M)	Run-19+20
9.8	4.5 (FXT)	589	0.9 days	100 M (108 M)	Run-20
7.3	3.9 (FXT)	633	1.1 days	100 M (117 M)	Run-20
19.5	6.2 (FXT)	487	1.4 days	100 M (118 M)	Run-20
13.5	5.2 (FXT)	541	1.0 day	100 M (103 M)	Run-20
5.75	3.5 (FXT)	666	0.9 days	100 M (116 M)	Run-20
4.59	3.2 (FXT)	699	2.0 days	100 M (200 M)	Run-19
3.85	3.0 (FXT)	721	4.6 days	100 M (259 M)	Run-18
3.85	7.7	420	11-20 weeks	100 M	Run-21

Table 2.1: Summary of all BES-II and FXT Au-Au beam energies $\sqrt{s_{\mathrm{NN}}}$, related baryon chemical potential μ_{B}, event statistics, run times, and date collected [53].

2.2.1 Event plane detector

This detector is described in more detail because it is used in this analysis.

The Event Plane Detector, which was fully installed and started gathering data in 2018, is designed to measure the current of charged particles that are created in heavy-ion collisions in range $0.7° < \theta < 13.5°$ ($2.14 < |\eta| < 5.09$) with respect to beam axis. This detector consists of two parts (east and west). Each of them is segmented into 12 supersectors consisting of 31 tiles, as can be seen in Fig. 2.5. All of the supersectors are connected by means of a bundle of 31 optical fibers which proceed to a silicon photomultiplier (SiPM) evaluating the incoming light and transferring it into electrical signal. Next, the signal is amplified and sent for processing in the STAR digitizing and acquisition system [54].

In general, one of the detector wheels can be segmented into 16 so-called rings. By one ring is meant a group of tiles lying in the same radius from the beam axis.

The event plane of a collision (see Chapter 4.1) is reconstructed via the azimuthal pattern of charged particles. The species or origin of a particle is not important in this case therefore the EPD does not have to be capable of particle identification.

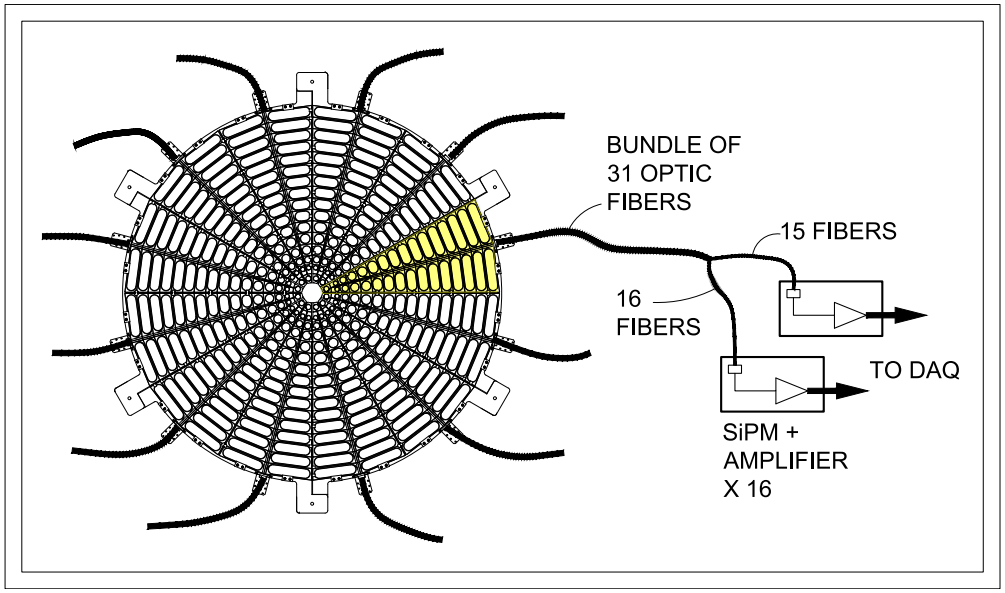

Figure 2.5: The scheme of EPD system where is depicted one of two EPD wheels [54].

Additionally, the magnetic field of 0.5 T bending the measured charged particles does not significantly affect the resulted event plane. Hence, all needed to be recorded by the EPD is a single hit point of each particle.

The relativistic charged particles in EPD pass through the plastic scintillator planes where they produce a signal. The measured signal distribution includes recognizable peaks corresponding to each minimally ionizing particles (MIPs) traversing the detector [54].

2.3 EIC

The Electron-Ion Collider (EIC) is a new planned construction at BNL in 2025 when the RHIC will be retired [55]. The EIC should start to operate in the early 2030s. The EIC will provide colliding polarized electrons with polarized light ions at high intensities. The EIC was launched as an official project in December 2019 when it was granted Critical Decision Zero (CD0) [56]. The estimated cost for the EIC is between 1.6 and 2.6 billion dollars and it should be constructed over ten years [57].

The future EIC will have to meet following requirements [56]:

- Polarized protons and electrons at a level of $\sim 70\%$
- The wide-ranging scale of ions from deuteron to uranium
- The CMS energies from 20-100 GeV for e-p collisions with the possibility of upgrades up to 140 GeV
- The value of electron-nucleon luminosity at least $10^{33} - 10^{34}$ cm^{-2}·s^{-1}

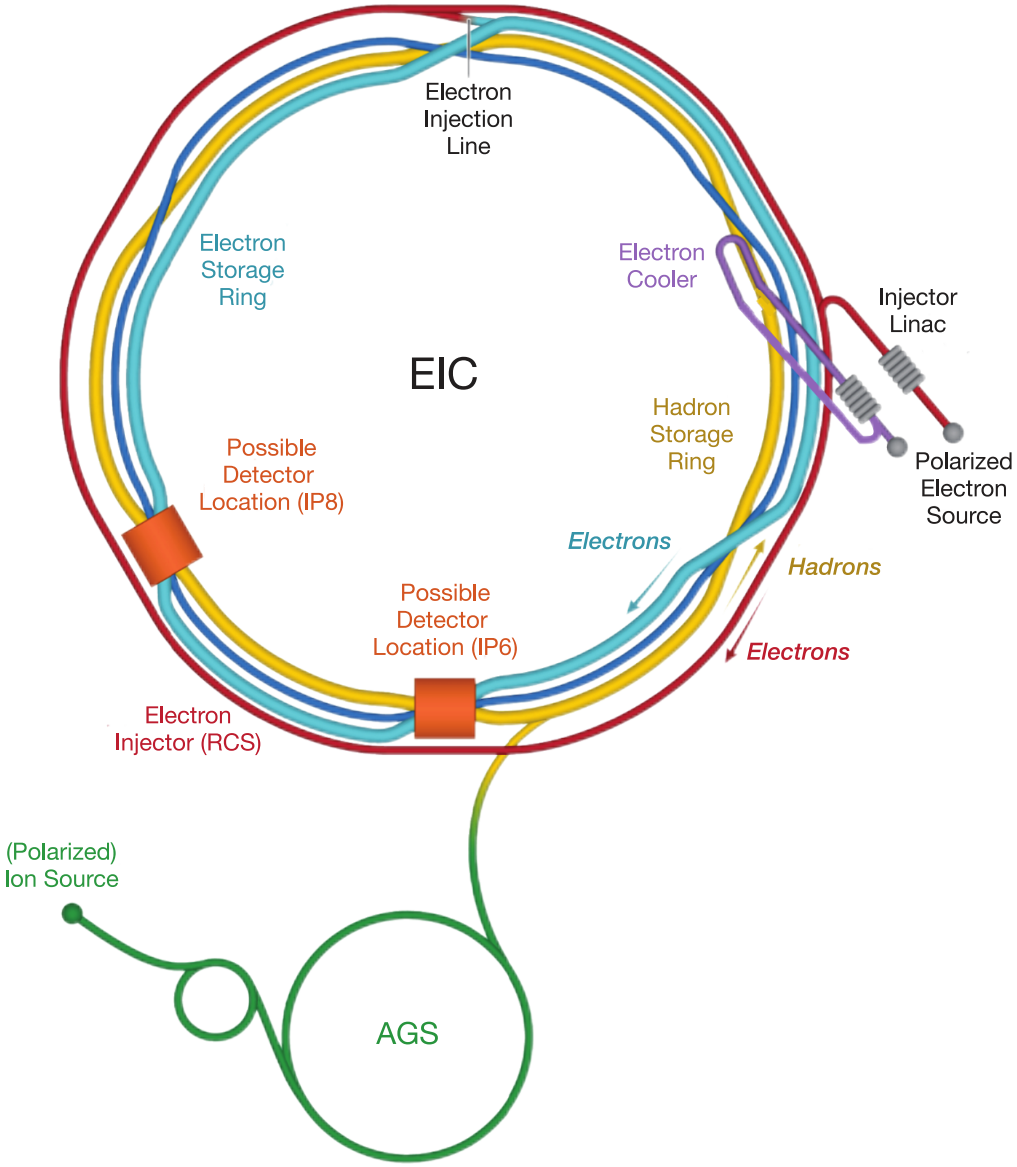

Figure 2.6: The scheme of the planned EIC accelerator [56].

The schematic of the EIC can be seen in Fig. 2.6 where the new additional Electron Storage Ring (cyan color), Polarized Electron source, Injector Linac and Electron Cooler are shown.

The new properties if colliding beams (electron-electron) also require a new suitable detectors. The EIC program can be completed by studying the inclusive, semi-inclusive and exclusive processes of electron-light/heavy nucleons, and polarized electron-light nuclei collisions. A proposal of central detector design meeting all requirements is shown as a 3D model in Fig. 2.7.

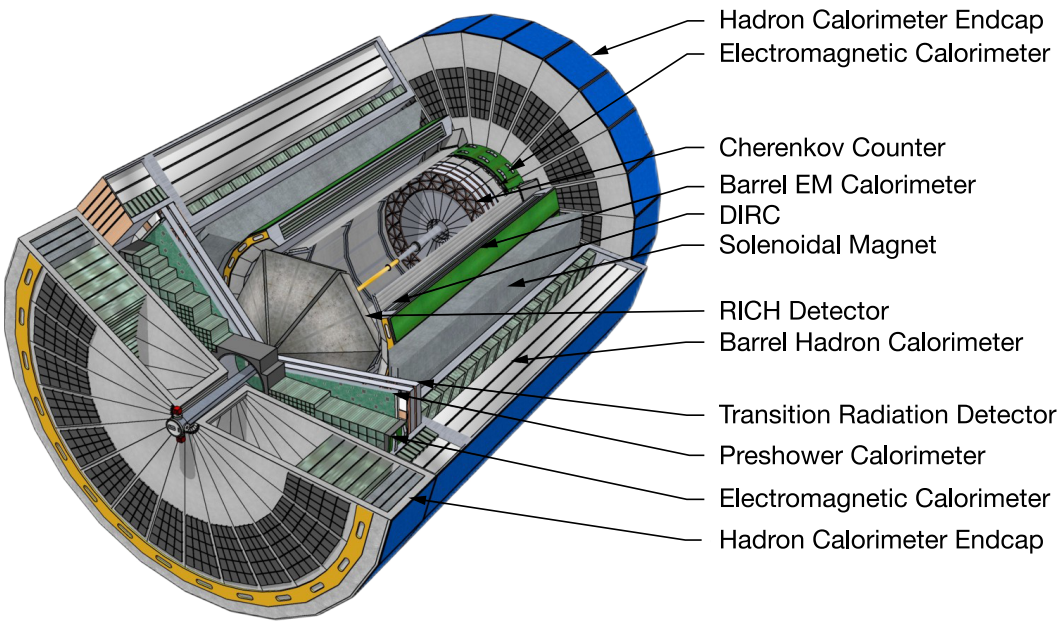

Figure 2.7: An illustration of a generic EIC concept detector [56].

The required pseudorapidity coverage of the concept detector is $|\eta| < 3.5$. Then it has to be able to precision tracking (resolution of 20 μm for all coordinates) and p-measurement (2% resolution for $p_{\mathrm{T}} > 0.1$ GeV/c), electron and hadron identification, and jet energy measurements [56].

Chapter 3

Dataset and reconstruction of Lambda hyperons

In this chapter, a description of the analyzed dataset, Λ hyperon, Kalman filter, and used selection criteria for Λ and $\overline{\Lambda}$ reconstruction will be discussed.

3.1 Dataset

In this work, data from Au-Au collisions at $\sqrt{s_{\mathrm{NN}}} = 27$ GeV from the STAR experiment are used. This dataset was produced in 2018 and its production tag is P19ib [58]. The used library is TFG21g which is the abbreviation of Tracking Focus Group, 21 indicates the year 2021 and the letter g describes the version. The overall number of events processed in this analysis is $6.068{\cdot}10^7$.

Λ and $\overline{\Lambda}$ particles are reconstructed using the Kalman filter described in more detail in the following section. In the Λ and $\overline{\Lambda}$ reconstruction, only the reconstructed particles with $p_{\mathrm{T}} > 0.5$ GeV/c are included. The particles are divided into 9 centrality bins (C_{ID}) describing different centrality ranges C, see Tab. 3.1, where $C_{\mathrm{ID}} = 0$ are most peripheral and $C_{\mathrm{ID}} = 8$ most central collisions.

C_{ID}	0	1	2	3	4	5	6	7	8
C [%]	80-70	70-60	60-50	50-40	40-30	30-20	20-10	10-5	5-0

Table 3.1: Division of centrality bins C_{ID} and related centrality ranges C.

3.2 Kalman filter

The Kalman filter (named after the Hungarian scientist Rudolf Emil Kálmán [59]) is a method used to optimally estimate particle traces. In principle, this filter performs prediction, and then it continues with a filter step.

The first step consists of extrapolation of the state vector to the subsequent k-th level of the detector. The state vector $\vec{r}$ is a vector of real independent numbers s_1,..., s_n describing for instance position (x, y, z), momentum (p_x, p_y, p_z), and energy E of the measured particle as follows

$$\vec{r} = (s_1, s_2, s_3, s_4, s_5, s_6) = (x, y, z, p_x, p_y, p_z, E). \tag{3.1}$$

First, one estimates approximation of the state vector in the first surface in the detector which measured the wanted particle. One denotes this state vector as r_0 and the related covariance matrix $\mathbb{C}_0$ can be chosen as

$$\mathbb{C}_0 = \mathbb{I} \cdot A \tag{3.2}$$

where $\mathbb{I}$ is an identity matrix and A is an arbitrary large positive number. Then the algorithm proceeds to the next surface. In general, the state vector $\vec{r}$ is changed between k-th and $(k+1)$-th surface as follows

$$\vec{r}_{k+1} = \mathbb{A}_{k+1}\vec{r}_k + \vec{\eta}_{k+1} \tag{3.3}$$

where $\mathbb{A}_k$ is a linear function (a matrix) describing the change of the state vector, called extrapolator and $\vec{\eta}_k$ is a random variable related to the noise of the measurement, such that

$$\langle \vec{\eta}_k \rangle = 0, \tag{3.4}$$

and is described by a covariance matrix

$$\mathbb{Q}_k = \langle \vec{\eta}_k \cdot \vec{\eta}_k^{\mathrm{T}} \rangle. \tag{3.5}$$

After that, one proceeds to the next $(k+1)$-th surface of the detector. If the new state vector $\vec{r}_{(k+1)}$ is different then the current estimation of the $\vec{k}$ is changed in the following way

$$\tilde{\vec{r}}_{k+1} = \mathbb{A}_{k+1}\vec{r}_k \tag{3.6}$$

$$\tilde{\mathbb{C}}_{k+1} = \mathbb{A}_{k+1}\mathbb{C}_k\mathbb{A}_{k+1}^{\mathrm{T}} + \mathbb{Q}_{k+1} \tag{3.7}$$

where $\tilde{\vec{r}}_{k+1}$ and $\tilde{\mathbb{C}}_{k+1}$ are an estimation of the state vector and the covariant matrix with respect to the previous k measurements, respectively [59].

In the filter step, the best estimation of the state vector according to all surfaces which have been already analyzed is chosen, i.e. first $k+1$ measurements. Then the algorithm proceeds to the next surface and the process is repeated [60].

An example of the reconstruction of particle track in 2D space is shown in Fig. 3.1 where the significant improvement of estimation with the increasing number of measurements with respect to the initial one can be seen.

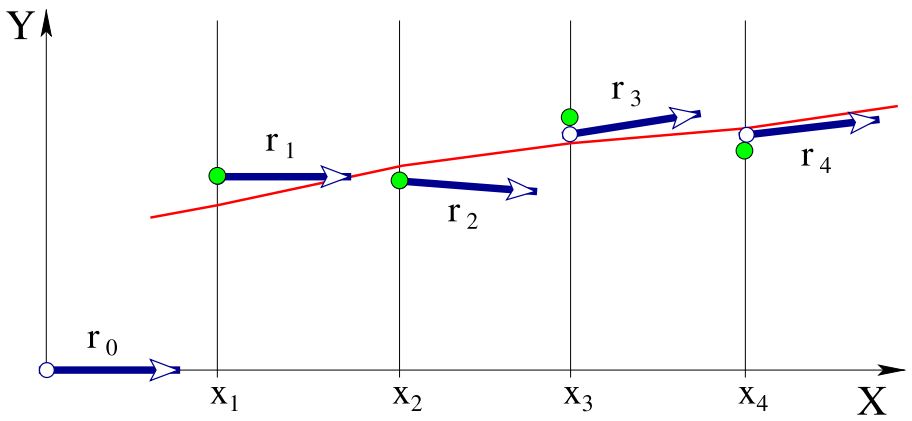

Figure 3.1: Scheme of the track fit where measured values are labeled as green dots, the state vector as white dots and the real track of particle as the red curve [60].

In general, this method includes following advantages [61]:

- No large matrices are included.
- Time of computation is proportional to the number of surfaces detecting the particle.
- The estimated track is not just extrapolation of the initial measured state vector. The reconstructed track is close to the real one.
- No requirement of linearity for all points of tracks, but only for the adjacent points.
- Optimal extrapolation of the track in foregoing and following detectors (calorimeters, vertex detectors, etc.).

Specifically, the KF particle finder (KFPF) package used in this analysis was first developed for CBM (Compressed Baryonic Matter) experiment. In 2012, the KFPF had implemented about 50 decay channels containing resonances, strange particles, multi-strange hyperons and charmed particles [62]. Currently, the KFPF includes above 100 decay channels, see Fig. 3.2, and it was successfully adapted to the STAR detector thanks to its geometry independence. The KFPF is able to estimate a wide range of parameters, such as position of particle decay, momentum, energy, mass, decay length and lifetime including their uncertainties [9], [63].

The package is written in ROOT which is an object oriented framework for data analysis written in C++. It was created for CERN where the amount of produced data was too enormous for any other programs (e.g. FORTRAN) [64].

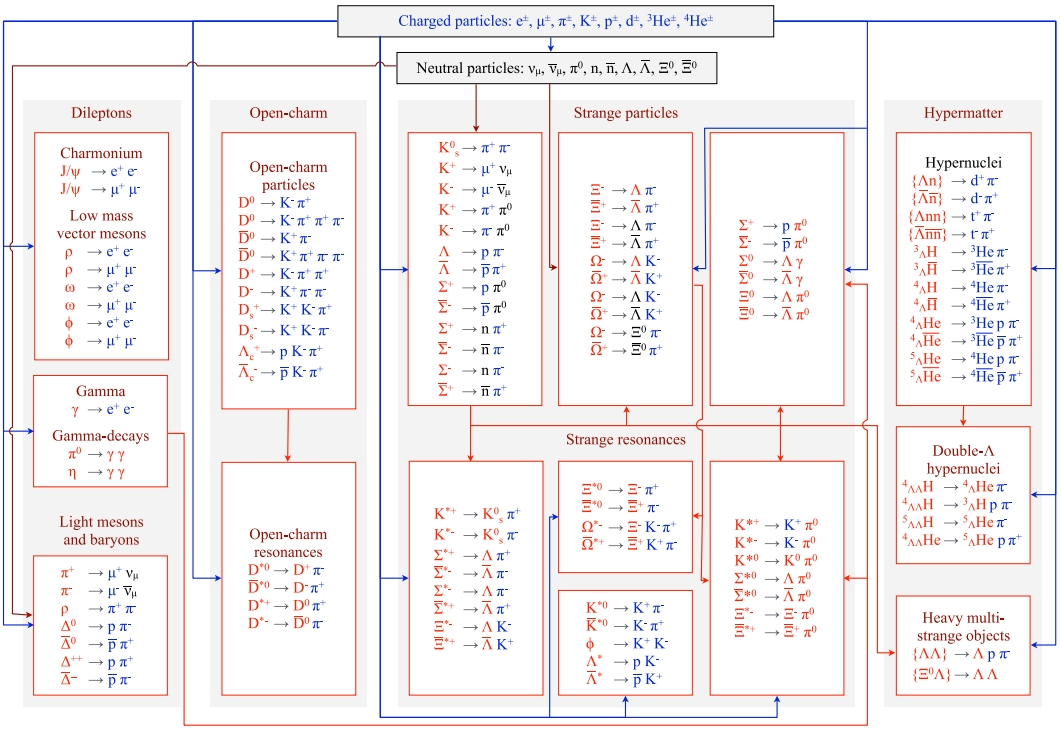

Figure 3.2: Block diagram of decay channels included in KFPF package [9].

3.3 Lambda hyperon

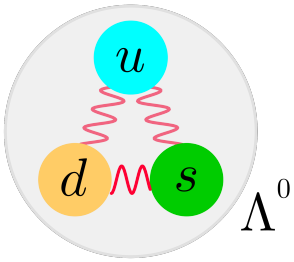

Figure 3.3: The lambda hyperon

Lambda particle (Λ) was discovered in 1950 by Anderson's group at Cal Tech. It is classified as a hyperon (i.e. baryon containing at least one strange quark and no heavier quarks) and a V-particle because its decay resembles a "V" shape in a bubble chamber [65].

Particle Λ and its antiparticle $\overline{\Lambda}$ consist of u, d and s-quark and $\overline{u}$, $\overline{d}$ and $\overline{s}$-quark, respectively. It is called a strange particle due to the relatively long mean lifetime $\tau = (2.632 \pm 0.020) \times 10^{-10}$ s [25] which was inexplicable in the time of discovery [66]. Its mass is $m_\Lambda = (1115.683 \pm 0.006)$ MeV [25] and it has no electric charge. It is a fermion because of the spin $\frac{1}{2}^+$. Izospin is zero. The main decay channels of Λ hyperon are included in Tab. 3.2.

Γ_i	Fraction (Γ_i/Γ)
$\Lambda \to p + \pi^-$	(63.9 ± 0.5) %
$\Lambda \to n + \pi^0$	(35.8 ± 0.5) %
$\Lambda \to n + \gamma$	$(1.75 \pm 0.15) \times 10^{-3}$

Table 3.2: First three decays modes of Λ hyperon [25].

The Λ hyperons can be found in nucleus. Such nuclei are called hypernuclei. These single- or double-Λ hypernuclei provide new information about strange hadronic matter and nΛ, pΛ and $\Lambda\Lambda$ interaction [67].

3.3.1 Reconstruction of Λ hyperon via KFPF

The Λ and $\overline{\Lambda}$ particles are reconstructed by means of the KF particle finder via the decay channels $\Lambda \to p + \pi^-$ and $\overline{\Lambda} \to \overline{p} + \pi^+$, respectively. However, not all of the reconstructed particles are real Λs ($\overline{\Lambda}$s). The so-called fake Λs are combinatorial background of random proton-pion pairs which can approach each other by a coincidence and they seem like the daughter of one particle. Therefore, for the Λ reconstruction, it is necessary to apply some selection criteria (see Fig. 3.4). Often used topological variables are:

- Proton to pion DCA[1] - maximum of acceptable DCA between daughter particles. The larger proton to pion DCA the more probably the particles are not from Λ decay.
- Λ decay length - minimum distance between the primary vertex and the decay point. The Λ decay point is expected to be displaced from the primary vertex.
- Proton/pion DCA - minimum of acceptable DCA between the primary vertex and the daughter particle. Particles that are close to the primary vertex could come from the different particle decays or they can be primary.
- Λ DCA - maximum of acceptable DCA between the primary vertex and the reconstructed track of Λ. The remoter Λ are probably not primary but can come from feed-down.

The topological KFPF selection criteria used in this analysis are gathered in Tab. 3.3 where d_{max} is maximum DCA between daughter particles, χ^2_{fit} is χ^2 of fit of daughter particle tracks describing whether the uncertainties of their trajectories are acceptable[2], χ^2_{topo} is χ^2 of the distance between the production point of the

[1] DCA - distance of closest approach

[2] The χ^2 for n measured values is defined as

$$\chi^2 = \sum_{i=1}^{n} \left(\frac{x_i - \mu_i}{\sigma_i} \right)^2 \tag{3.8}$$

where x_i, μ_i and σ_i are the i-th measured and fitted value and its standard deviation, respectively.

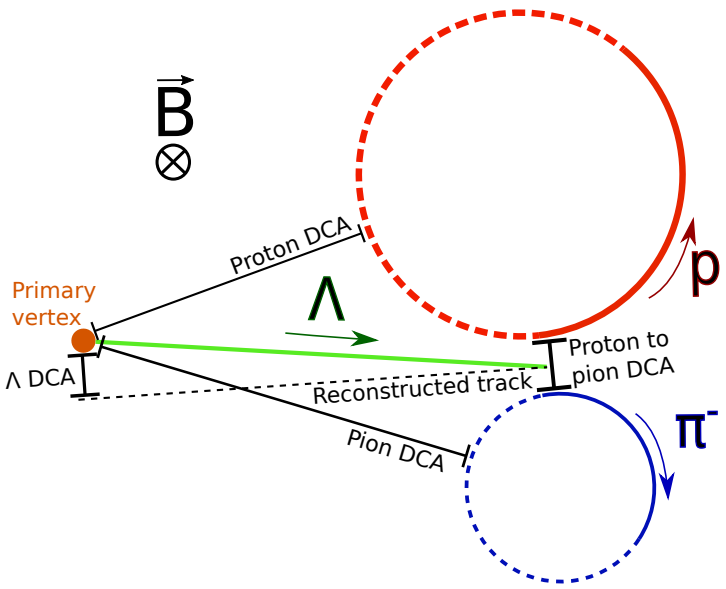

Figure 3.4: Scheme of a decay of Λ hyperon into related proton and pion in a magnetic field of detector.

mother particle and the primary vertex, l is a decay length of the mother particle, dl is the uncertainty of the decay length, and χ^2_{prim} is criterion to distinguish between secondary and primary particles which is defined as

$$\chi^2_{\text{prim}} = \Delta\vec{r}^{\text{T}}(C_{track} + C_{PV})^{-1}\Delta\vec{r} \tag{3.9}$$

where $\Delta\vec{r}$ is difference between the primary vertex position and the track, C_{track} is a covariance matrix of the reconstructed track and C_{PV} is a covariance matrix of the reconstructed primary vertex position [68].

d_{max} [cm]	χ^2_{fit}	l [cm]	$l/\text{d}l$	χ^2_{topo}	χ^2_{prim}
<1	<10	>5	>5	<5	>18.6

Table 3.3: Default KFPF selection criteria. See text for more details.

Nevertheless, some secondary Λ hyperons are reconstructed as well. By secondary particle one means Λ hyperons which are daughter of heavier particles, e.g. Σ^+, Σ^0, Σ^-, Ω^-, Ξ^0, Ξ^-, etc. [25]. As was already mentioned in subsection 5.2.1, these daughter Λ hyperons as well as the fake ones can influence the measured global Λ polarization. The Λ ($\overline{\Lambda}$) are reconstructed using an invariant mass method - pairing of all identified pion and proton candidates.

The invariant mass of Λ ($\overline{\Lambda}$) candidates was fitted by a double Gaussian distribution

$$G(x) = A_1 \exp\left[-\frac{1}{2}\left(\frac{x-\mu_1}{\sigma_1}\right)^2\right] + A_2 \exp\left[-\frac{1}{2}\left(\frac{x-\mu_2}{\sigma_2}\right)^2\right] \tag{3.10}$$

where $A_{1,2}$ are amplitudes, $\mu_{1,2}$ and $\sigma_{1,2}$ are the mean values and the standard deviations of the related Gaussian distribution, respectively. The overall mean value

of the Λ signal is estimated as follows

$$\mu = \frac{A_1\mu_1\sigma_1 + A_2\mu_2\sigma_2}{A_1\sigma_1 + A_2\sigma_2} \tag{3.11}$$

and the overall standard deviation is

$$\sigma = \sqrt{\frac{A_1\sigma_1(\sigma_1^2 + \mu_1^2) + A_2\sigma_2(\sigma_2^2 + \mu_2^2)}{A_1\sigma_1 + A_2\sigma_2} - \mu^2}. \tag{3.12}$$

The background of the Λ ($\overline{\Lambda}$) candidates was fitted by the polynomial of the second order

$$\mathrm{pol2}(x) = ax^2 + bx + c. \tag{3.13}$$

The double Gaussian distribution $G(x)$ was fitted in the invariant mass range 1.10 GeV/c^2 < M_{inv} < 1.13 GeV/c^2 and the background pol2(x) in the full range except 1.11 GeV/c^2 < M_{inv} < 1.12 GeV/c^2. These ranges were used as initial values for the final fit of the invariant mass by $G(x)$ + pol2(x).

The background yield B is defined as

$$B = \frac{\int_{\mu-3\sigma}^{\mu+3\sigma} \mathrm{pol2}(x)\ \mathrm{d}x}{b_w} \tag{3.14}$$

where b_w is the bin width. The signal yield was computed as follows

$$S = \frac{\int_{\mu-3\sigma}^{\mu+3\sigma} G(x)\ \mathrm{d}x}{b_w}. \tag{3.15}$$

The signal-to-background yield ratio S/B is just their proportion. The related uncertainties are computed via ROOT function *IntegralError*.

An example of the above-mentioned procedure can be seen in Fig. 3.5. To evaluate the quality of the fit, the pull distribution $g_i(x)$ is used, defined as

$$g_i(x) = \frac{x_i - f(x_i)}{\sigma(x_i)} \tag{3.16}$$

where x_i is the i-th measured value, $f(x_i) = G(x_i) + \mathrm{pol2}(x_i)$ and the $\sigma(x_i)$ is the uncertainty of the fit.

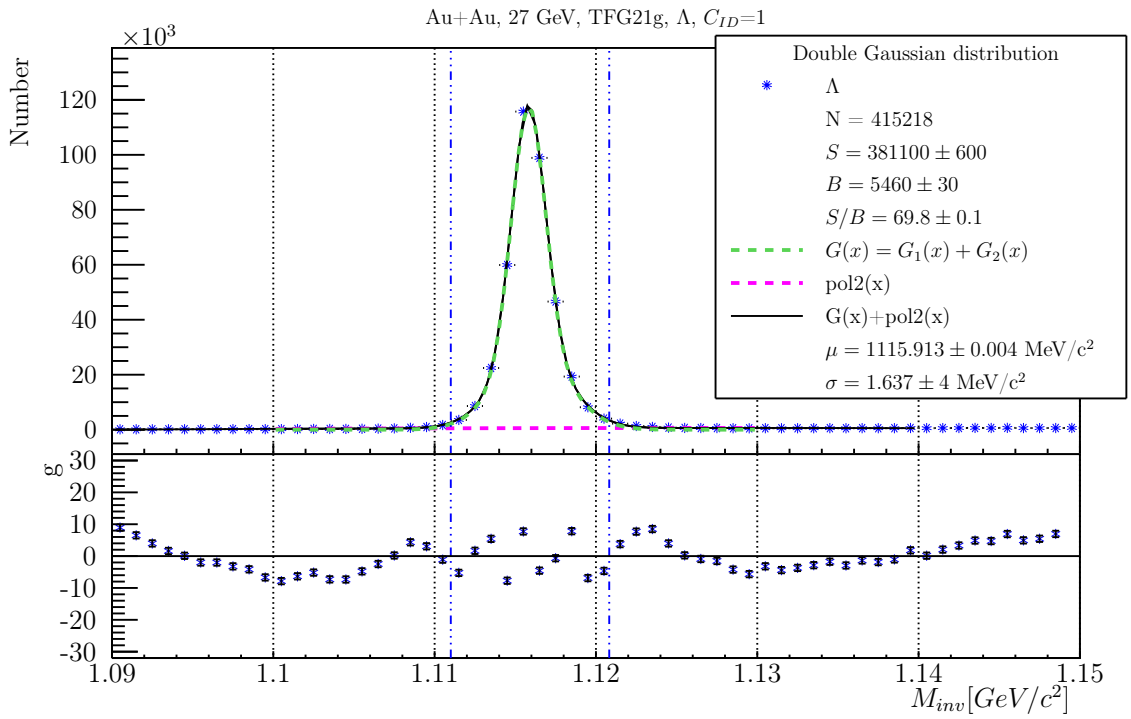

Figure 3.5: The invariant mass distribution of Λ hyperon candidates with $p_{\mathrm{T}} > 0.5$ GeV/c for centrality bin 60-70% where N is number of all reconstructed candidates, S is signal yield, B is the background, S/B is their ratio. For more detail see text.

Chapter 4

Reconstruction of the first order event plane

In this chapter, the event plane, steps needed for its reconstruction, the computation of its resolution, and different corrections will be discussed.

4.1 Event plane

One of the important ingredients to compute the Λ polarization is determination of the so-called event plane (EP). The event plane is closely related to the reaction plane (RP) which is illustrated in the Fig. 4.1 and which is defined by two vectors: direction of the beam (z-axis) and the impact parameter $\vec{b}$. The angle of the reaction plane Ψ_R with respect to the laboratory axis can not be measured directly because the impact parameter cannot be measured directly. One can say that the event plane is an experimental estimation of the RP.

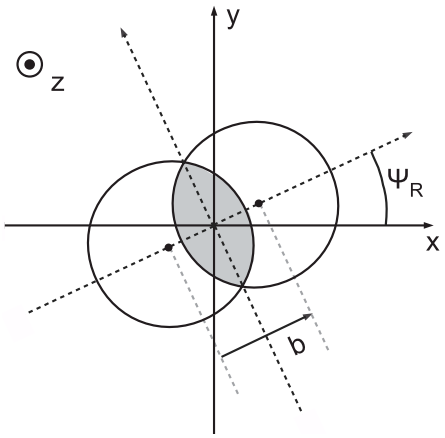

Figure 4.1: The scheme of the reaction plane in a non-central collision of two nuclei where $\vec{b}$ is the impact parameter and Ψ_R is an angle of the reaction plane. [69]

The resolution of the EP is limited by the finite number of produced particles and the fluctuations of their multiplicity for the fixed orientation of EP [70]. Hence,

the difference between RP and EP. One way to determine the EP is by using the so-called event flow vector $\vec{Q}_n$ (or Q-vector) which is defined as follows

$$\vec{Q}_n = \begin{pmatrix} Q_x \\ Q_y \end{pmatrix} = \begin{pmatrix} \sum_i w_i \cos n\phi_i \\ \sum_i w_i \sin n\phi_i \end{pmatrix} \tag{4.1}$$

where ϕ_i is the azimuthal angle of i-th produced particle and w_i is an associated weight. The most common choice of this weight maximizes the EP resolution. The event plane angle Ψ_n of the n-th harmonic (or the n-th order) can be obtained by equation

$$\Psi_n = \frac{\arctan\left(\frac{Q_y}{Q_x}\right)}{n} = \frac{\arctan\left(\frac{\sum_i w_i \sin n\phi_i}{\sum_i w_i \cos n\phi_i}\right)}{n}. \tag{4.2}$$

It should be noted that n-th EP angle Ψ_n lies in the range of $\langle 0; 2\pi/n)$ [71].

The EPD detector at STAR (see Chapter 2.2.1) can be used for the reconstruction of the EP. There one can choose the weights w_i as follows

$$w_i = \begin{cases} 0 & nMIP < Min \\ nMIP & Min \leq nMIP < Max \\ Max & nMIP \geq Max \end{cases} \tag{4.3}$$

where nMIP is the number of minimum ionizing particles which have two thresholds, i.e. $Min = 0.3$ because of a dark signal and $Max = 3$ to suppress Landau fluctuations.

The nMIP can be computed from ADC (analog-to-digital converter) signal which is measured on each tile in the EPD. If one assumes a linear dependence of the particle energy loss E in the scintillator on the ADC value, then

$$E = G \cdot (ADC + O) \tag{4.4}$$

where G is a gain and O is a offset. Both of these constant values have to be calibrated. However, energy loss is not the point of interest in this case. The wanted information is the number of particles, which can be obtained as

$$nMIP = \frac{ADC + O}{MPV} \tag{4.5}$$

where MPV is the most probable value for the one MIP Landau distribution [72].

In ideal case, the EP can be obtained by Eq. (4.2). Nevertheless, the EPD's tiles do not have the same sensitivity and there are also other effects which can negatively influence the reconstruction of the EP, therefore one can use additional corrections to improve the resolution of the EP:

- Phi-weighting - different weights for each EPD's tiles
  - Ring-weighting - different weights of signal w.r.t. ring or ring groups of the EPD
  - Eta-weighting - different weights of signal w.r.t. pseudorapidity of the produced particles
- Recentering - the Q-vectors are averaged over large sample of events [73].
- Psi-shifting - flattening of the EP distribution

4.1.1 Phi-weighting

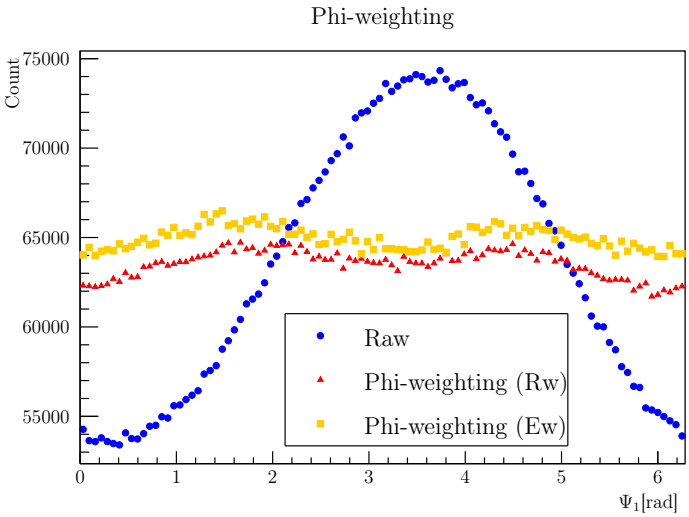

Figure 4.2: Comparison of raw Ψ_1 and phi-weighted Ψ_1 distribution for Au-Au collisions at energy $\sqrt{s_{\mathrm{NN}}} = 27$ GeV where *Rw* is the ring-weighting and *Ew* is the eta-weighting.

The measured Ψ_1 distribution has to be isotropized which can be done by a so-called phi-weighting correction which is trivial to introduce in the case of a finite-element system (e.g. EPD). One assumes an azimuthal angle symmetry of the particle flux for each ring of the EPD in case the measured signal is averaged over a large sample of events. The next assumption is the proportionality of the measured signal on each detector tile to the flux in an event. As a reminder, the measured ADC signal from EPD is proportional to the chosen weight w_i in Eq. (4.2) except the lowest and the highest values. One can consider the anisotropy of $\mathrm{d}w_i/\mathrm{d}\phi$ as an inefficiency which can be corrected by b_k coefficients which depend on the azimuthal angle ϕ and on the tile in case of the EPD. The b_k coefficient is introduced as follows

$$b_{k,r} \equiv \frac{\langle w_k \rangle_k}{\langle \langle w_k \rangle_k \rangle_r} \tag{4.6}$$

where k and r denote k-th tile and the ring related to k-th tile of the EPD, respectively, and the angle brackets $\langle \dots \rangle_{k \text{ or } r}$ denote the mean value for k-th tile or all tiles in the ring r for a large sample of events. The corrected w'_k is then

$$w'_k = \frac{w_k}{b_k}. \tag{4.7}$$

The scattering of the produced particles in the upstream material of the detector is the main source of the observed anisotropy. The scattering causes a multiplying effect, i.e. the number of the observed particles can be greater than their real number ($b_k > 1$). As was shown, this correction is strong tool enough that the reasonable results can be obtained without any other corrections [74].

An example of using the phi-weighting of the Ψ_1 distribution can be seen in Fig. 4.2 where just 4 inner rings (see paragraph 4.1.2 Ring-weighting) for ring-weighting (Rw) were considered.

4.1.2 Ring-weighting

This method considers different weights for each ring or ring-groups (RGs) of EPD. It was shown for Au-Au collisions at 27 GeV that each ring is correlated with the adjacent rings at the value of a few percent and that the inner first 5 rings are most correlated through the entire group [75]. The outer rings (12 - 16) are also correlated with each other but they are anticorrelated with the inner group of rings. These observation are related to flow and antiflow of spectators and participants, respectively. The intermediate rings (6 - 11) can be described as a transition region and they weakly correlate with the inner and outer rings [75].

One can introduce the ring weights Z_r into Eq. (4.2) for $n = 1$ as follows

$$\Psi_1 = \arctan\left(\frac{\sum_{r=1}^{16} Z_r \sum_{i\in r} w_i \sin\phi_i}{\sum_{r=1}^{16} Z_r \sum_{i\in r} w_i \cos\phi_i}\right). \tag{4.8}$$

where some weights Z_r can be chosen for instance as zero in order to neglect some problematic rings. This correction may be used just for the first iteration and then instead of them the eta-weighting can be used.

The most optimal set of Z_r can be found by maximizing the resolution of the event plane, see Eq. 4.21, or minimizing following value

$$\xi = 1 - \sqrt{\langle\cos[(\Psi_1^E - \Psi_1^W)]\rangle} \tag{4.9}$$

where we consider first-order EP and E and W denote east and west wheel of the EPD, respectively. The square root in the Eq. 4.9 can be omitted because the resolution is a positive value and the square root is an increasing function for these values. This problem is suited for the CERN library MINUIT (Function Minimization and Error Analysis [76]). Actually, only the relative weights Z_r between rings or RGs are important to the analysis, thus one of the weight can be chosen as 1.

4.1.3 Eta-weighting

Alternatively to the ring-weighting, more general eta-weighting can be used. In this case we consider v_1 depending on the centrality C and pseudorapidity η as a weight for the measured particles in the EPD. The easiest way how to capture both of the mentioned dependencies is to divide the data with respect to the centrality of collisions and then fit the v_1 dependence on η with the polynomial of the third order

$$v_1(\eta, C) = a\eta^3 + b\eta^2 + c\eta + d. \tag{4.10}$$

The quadratic coefficient b can be neglected because it is always approximately zero and the constant coefficient d is usually negative and low with respect to the other terms in Eq. 4.10 thus can be also neglected [77]. Hence, the final weight for particles is

$$v_1(\eta, C) = a\eta^3 + c\eta. \tag{4.11}$$

However, the knowledge of the v_1 is needed for this type of weighting. Therefore, the optimal way to compute the angle of EP Ψ_1 using this correction is to use the ring-weighting for the first iteration (for instance there one can consider just the inner rings), to compute the a and c coefficients, and after that to use the eta-weightings. In fact, there is nothing like a wrong choice of weights because the worse choice just provides a worse resolution.

4.1.4 Psi-shifting

The main goal of this correction is to flatten the Ψ_1 distribution. The corrected Ψ_1' can be introduced as

$$\Psi_1' = \Psi_1 + \Delta\Psi_1 \tag{4.12}$$

where the term $\Delta\Psi_1$ is defined as

$$\Delta\Psi_1 = \sum_n \left[A_n \cos(n\Psi_1) + B_n \sin(n\Psi_1)\right]. \tag{4.13}$$

As can be seen from the Eq. (4.12), Ψ_1 is fully corrected when the term $\Delta\Psi_1$ equals zero. Hence, the terms in the Eq. (4.13) are subtracted from each other for all n or alternatively

$$A_n = -\frac{2}{n}\langle\sin(n\Psi_1)\rangle \tag{4.14}$$

$$B_n = \frac{2}{n}\langle\cos(n\Psi_1)\rangle, \tag{4.15}$$

where the angle brackets $\langle\dots\rangle$ denote the mean value for a large sample of events. Consequently, the Eq. (4.12) can be expressed as

$$\Psi_1' = \Psi_1 + \sum_n \frac{2}{n}\left(-\langle\sin(n\Psi_1)\rangle\cos(n\Psi_1) + \langle\cos(n\Psi_1)\rangle\sin(n\Psi_1)\right). \tag{4.16}$$

Frequently, the sum is computed up to the fourth harmonic ($n = 4$) because the higher terms are mostly too low to have any effect on the RP resolution [78]. To reach the flattest Ψ_1 distribution it is good to use this correction more times in iterations.

An example of applying the psi-shifting together with the phi-weighting on the Ψ_1 distribution can be seen in Fig. 4.3 where just 4 inner rings for ring-weighting (Rw) were considered.

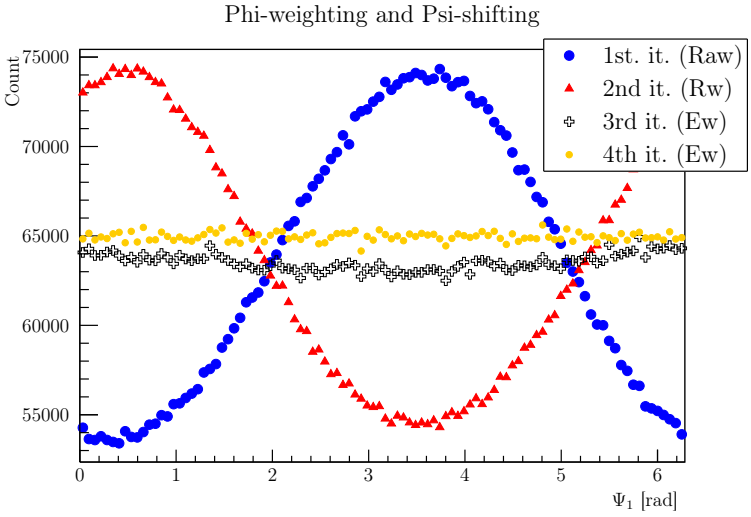

Figure 4.3: Comparison of raw Ψ_1 and phi-weighted + psi-weighted Ψ_1 distribution for Au-Au collisions at energy $\sqrt{s_{\mathrm{NN}}} = 27$ GeV where Rw and Ew mean ring-weighting and eta-weighting, respectively.

4.1.5 Recentering

This correction can be perceived as normalization of the measured Q-vectors and it is more practical than the other because it provides zero average of the Q-vectors. It can deal with the situation that some part of the detector does not work but it is less sensitive to strong acceptance variations [73].

The normalization depends on the used corrections. In the case of all corrections (phi-weighting, psi-shifting and ring- or eta-weighting), the normalized Q'_1-vector has following form

$$\vec{Q'_1} = \frac{\vec{Q_1}}{\sum_i Z_i w'_i} \tag{4.17}$$

where Z_i is ring- or eta-weight of i-th particle and w'_i denotes phi-weight corrections. If one does not consider ring- or eta-weighting and phi-weighting then for all i $Z_i = 1$ and $w'_i = w_i$, respectively.

4.1.6 Summary of the corrections

In this analysis, all of the above-mentioned corrections are used. The recentering is performed always including the raw data. The final EP Ψ_1 angles used for the global Λ polarization computation is presented in Fig. 4.3. It includes: 4 iterations including recentering, phi-weighting, eta-weighting, and psi-shifting.

4.2 Resolution of the event plane

As it was already mentioned, the finite multiplicity of the produced particles limits the accuracy of the EP estimation. The EP resolution for n harmonic is defined by

$$\mathscr{R}_n = \langle \cos\left[n(\Psi_n - \Psi_{\mathrm{RP}})\right] \rangle \tag{4.18}$$

where the angle brackets $\langle \dots \rangle$ denote the mean value for a large sample of events. The right side of Eq. (4.18) can be computed as follows

$$\mathscr{R}_n(\chi) = \frac{\sqrt{2}}{2}\chi \exp\left(-\frac{\chi^2}{2}\right)\left[I_{\frac{n-1}{2}}\left(\frac{\chi^2}{2}\right) + I_{\frac{n+1}{2}}\left(\frac{\chi^2}{2}\right)\right] \tag{4.19}$$

where I_k is the modified Bessel function of the first kind and the dimensionless parameter χ is

$$\chi = v_n\sqrt{N} \tag{4.20}$$

where v_n is the n-th order flow coefficient and N is the multiplicity of produced particles [73]. The dependence of $\mathscr{R}_1$ on χ can be seen in Fig. 4.4. One can estimate the EP resolution by dividing the full event into two independent sub-events A and B with equal multiplicity. The resolution of the sub-events has following form

$$\mathscr{R}_{n,sub} = \sqrt{\langle \cos[n(\Psi_n^A - \Psi_n^B)] \rangle}, \tag{4.21}$$

i.e. the square root of the above-mentioned correlation because both of sub-events are positively correlated. This is based on the fact that each sub-event is correlated with the RP [79]. The coefficient χ_{sub} can be computed from Eq. (4.19) for a given $\mathscr{R}_{n,sub}$ by iteration. Then the last step to get the full EP resolution is following

$$\mathscr{R}_{n,full} = \mathscr{R}(\sqrt{2}\chi_{sub}) \tag{4.22}$$

where the Eq. (4.19) is used.

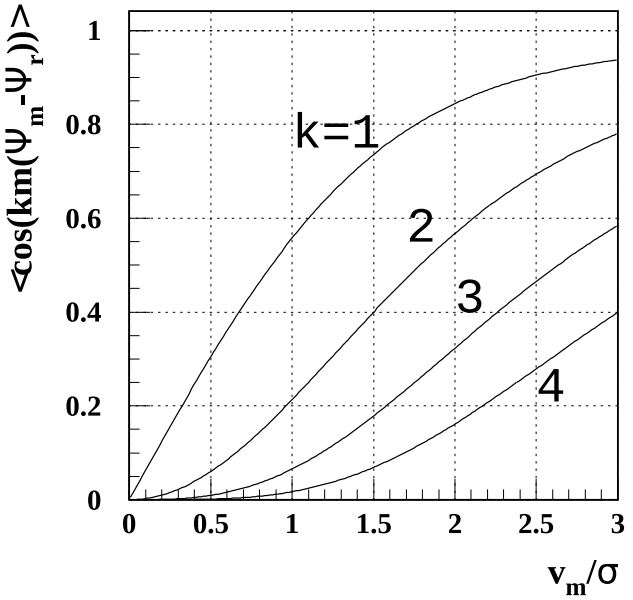

Figure 4.4: The event plane resolution of n-th ($n = km$) harmonic of the particle distribution with respect to $\chi_m = v_m\sigma = v_m\sqrt{N}$ where N is multiplicity of the produced particles and σ its standard deviation [79].

If the first order EP resolution is low (<0.5) then the Eq. (4.22) is approximately

$$\mathscr{R}_{1,full} \approx \sqrt{2}\mathscr{R}_{sub} \tag{4.23}$$

because the parameter χ is proportional to $\sqrt{N}$ and the full event consists of two times more particles than the sub-event [73]. However, in this work, the full Eq. (4.22) is preferred.

An example of the first order EP resolution for Au-Au collisions at energy $\sqrt{s_{\mathrm{NN}}} =$ 27 GeV can be seen in Fig. 4.2 where just 4 inner rings for ring-weighting (Rw) were considered.

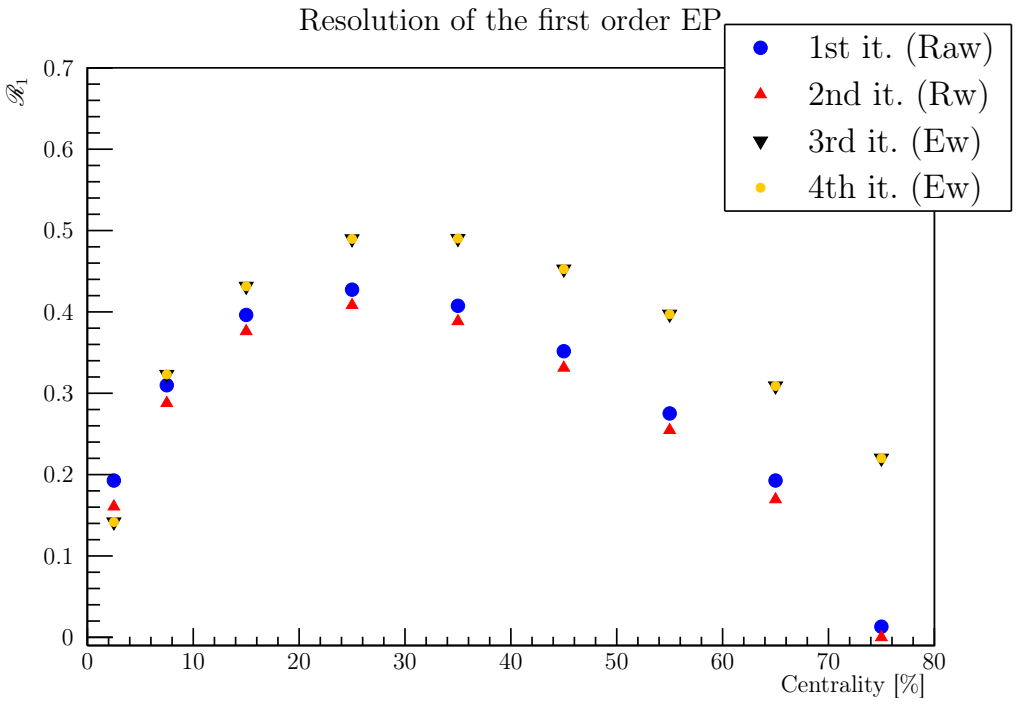

Figure 4.5: Comparison of the resolution of the first order event planes $\mathscr{R}_1$ with respect to centrality of collisions including recentering, phi-weighted, psi-shifting, ring-weighting (Rw), and eta-weighting (Ew) for Au-Au collisions at energy $\sqrt{s_{\mathrm{NN}}} =$ 27 GeV. The results are for 4 iterations.

The final distribution used in this analysis is the 4th iteration which is related to the 4th iteration in Fig. 4.3.

Chapter 5

Daughter proton angular distribution and global lambda polarization

In this chapter, analysis of Λ ($\overline{\Lambda}$) polarization via daughter proton angular distribution and the manners to extract global Λ ($\overline{\Lambda}$) polarization will be described.

Recall, that the global Λ ($\overline{\Lambda}$) polarization can be computed as follows

$$P_H = \frac{8}{\pi \alpha_H} \frac{\langle \sin\big(\Psi_1 - \phi_p^*\big) \rangle}{\mathscr{R}_1} \tag{5.1}$$

where Ψ_1 is the first order event plane, $\mathscr{R}_1$ is its resolution and ϕ_p^* is azimuthal angle of the daughter particle in the rest frame of mother hyperon.

The computed resolutions $\mathscr{R}_1$ for Au-Au collisions at energy $\sqrt{s_{\mathrm{NN}}} = 27$ GeV and for $p_{\mathrm{T}} > 0.5$ GeV/c are introduced in Tab. 5.1. Next, one considers the decay constants $\alpha_\Lambda = 0.732 \pm 0.014$ and $\alpha_{\overline{\Lambda}} = -0.758 \pm 0.010$ for Λ and $\overline{\Lambda}$, respectively [25].

C [%]	80-70	70-60	60-50	50-40	40-30	30-20	20-10	10-5	5-0
$\mathscr{R}_1$	0.2286	0.3173	0.4074	0.4643	0.5028	0.5056	0.4525	0.3520	0.2140

Table 5.1: The resolution of the first order EP $\mathscr{R}_1$ for each centrality range C.

5.1 Proton angular distribution

To obtain the Λ ($\overline{\Lambda}$) polarization, one has to reconstruct the angular distribution of daughter baryons, ϕ, which has to be boosted to the rest frame of the mother particle ϕ^*. Then one uses the angle of the reconstructed event plane (see Chapter 4.1) to find the angular distribution with respect to the event plane of the collision $(\Psi_1 - \phi^*)$. Together with the computed resolution of the event plane $\mathscr{R}_1$ in Fig. 4.5 one has all values needed for the global polarization in Eq. (1.5)

Raw ϕ distributions of daughter protons (antiprotons) from Λ ($\overline{\Lambda}$) decays as a function of their azimuthal angle in the laboratory frame for Au-Au collisions at

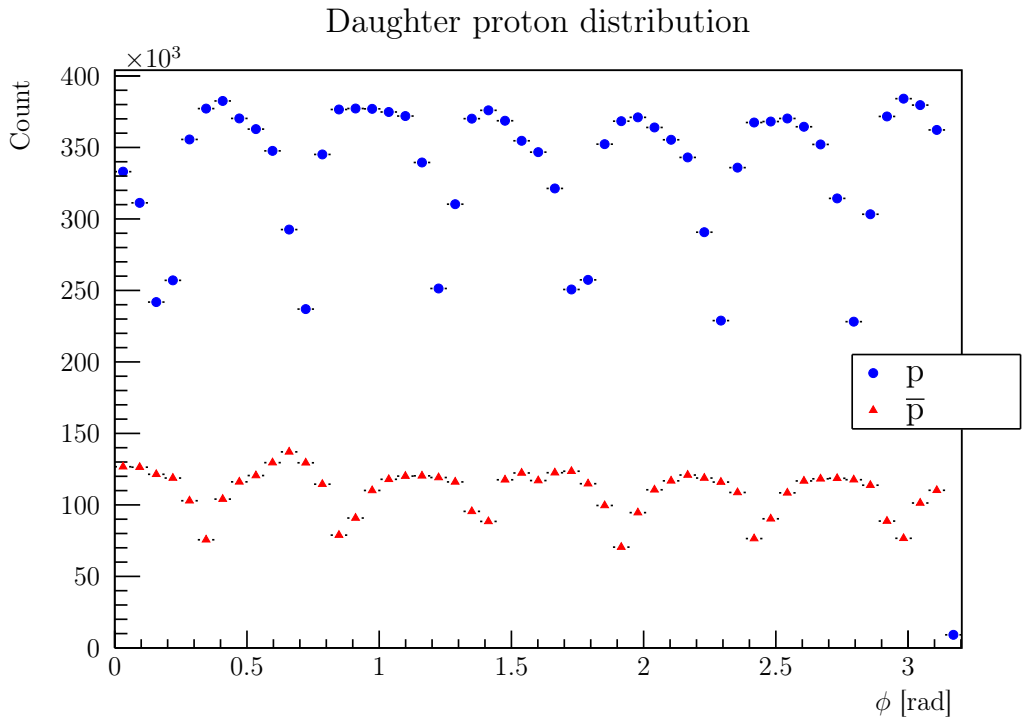

Figure 5.1: The angular distribution of daughter protons (p) and antiprotons ($\overline{p}$) for Au-Au collisions at $\sqrt{s_{\mathrm{NN}}} = 27$ GeV.

energy $\sqrt{s_{\mathrm{NN}}} = 27$ GeV can be seen in Fig. 5.1. The periodic minima observed in the proton and antiproton distribution are related to the construction of TPC that is segmented and some parts of it have low sensitivity.

The next step is the boost of the daughter protons (antiprotons) to the rest frame of the mother Λ ($\overline{\Lambda}$) particle. This can be done using following equations

$$\begin{pmatrix} E' \\ p'_x \\ p'_y \\ p'_z \end{pmatrix} = \begin{pmatrix} \gamma & -\gamma\beta_x & -\gamma\beta_y & -\gamma\beta_z \\ -\gamma\beta_x & 1+(\gamma-1)\frac{\beta_x^2}{\beta^2} & (\gamma-1)\frac{\beta_x\beta_y}{\beta^2} & (\gamma-1)\frac{\beta_x\beta_z}{\beta^2} \\ -\gamma\beta_y & (\gamma-1)\frac{\beta_y\beta_x}{\beta^2} & 1+(\gamma-1)\frac{\beta_y^2}{\beta^2} & (\gamma-1)\frac{\beta_y\beta_z}{\beta^2} \\ -\gamma\beta_z & (\gamma-1)\frac{\beta_z\beta_x}{\beta^2} & (\gamma-1)\frac{\beta_z\beta_y}{\beta^2} & 1+(\gamma-1)\frac{\beta_z^2}{\beta^2} \end{pmatrix} \cdot \begin{pmatrix} E \\ p_x \\ p_y \\ p_z \end{pmatrix} \tag{5.2}$$

where E is energy of the particle, $\vec{p} = (p_x, p_y, p_z)$ is its momentum, $\vec{\beta} = (\beta_x, \beta_y, \beta_z) = (v_x, v_y, v_z)$ is velocity of the mother particle and $\gamma = \frac{1}{\sqrt{1-\beta^2}}$. The angle of the boosted daughter particle is then

$$\phi^* = \arctan\left(\frac{p'_y}{p'_x}\right). \tag{5.3}$$

The angular distribution of daughter protons (antiprotons) in the rest frame of their mother particle is presented in Fig 5.2.

C [%]	80-70	70-60	60-50	50-40	40-30	30-20	20-10	10-5	5-0
a	0.1608	0.1600	0.1600	0.1595	0.1457	0.1369	0.1092	0.0772	0.0700
c	-1.950	-1.900	-1.850	-1.706	-1.438	-1.340	-1.045	-0.717	-0.700

Table 5.2: The cubic a and linear c coefficients for centrality ranges C used in eta-weighting.

The next step is to obtain the angular distribution of the boosted daughter particles with respect to the event plane $\Psi_1 - \phi^*$, as can be seen in Fig. 5.3. The reconstructed EP includes phi-weighting, psi-shifting, recentering and eta-weighting with parameters gathered in Tab. 5.2, see Chapter 4.1 for more details.

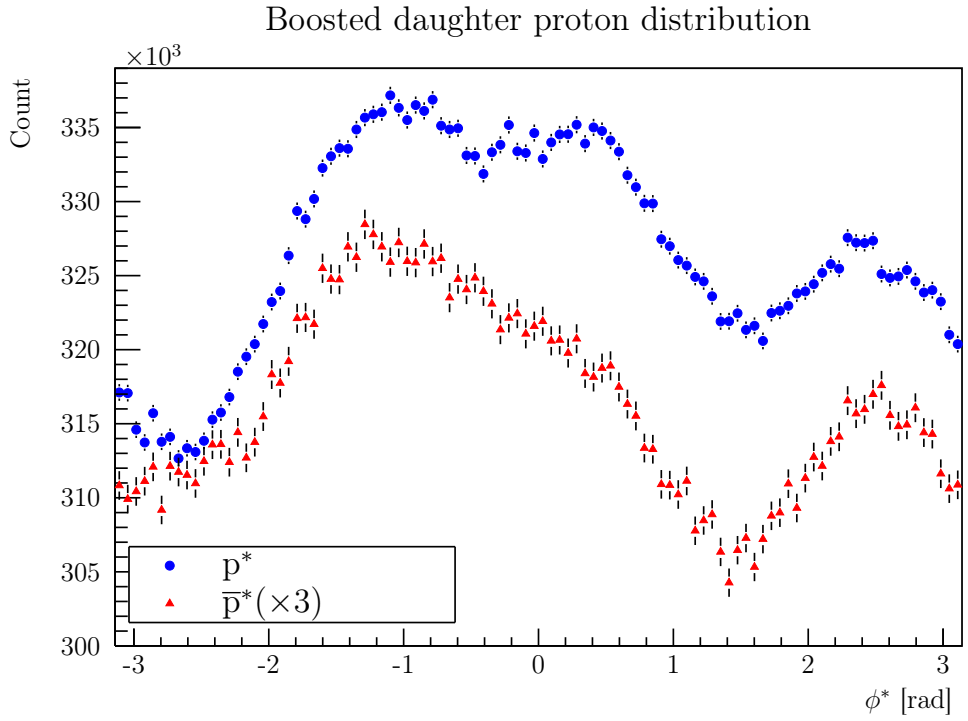

Figure 5.2: The angular distribution of daughter protons (p) and antiprotons ($\overline{p}$) in Λ ($\overline{\Lambda}$) rest frame ϕ^* for Au-Au collisions at $\sqrt{s_{\mathrm{NN}}} = 27$ GeV.

The linear and cubic parameters in Tab. 5.2 are from previous analysis by STAR [80]. As was mentioned in Chapter 4.1, these parameters are related to the flow coefficients v_1 which are different for each centrality range.

The final distribution $\Psi_1 - \phi^*$ can be used in Eq. (5.1) to compute the global polarization of Λ ($\overline{\Lambda}$). However, the polarization is contaminated by the background. Therefore, the invariant mass method or event plane method are applied in order to subtract the background contribution.

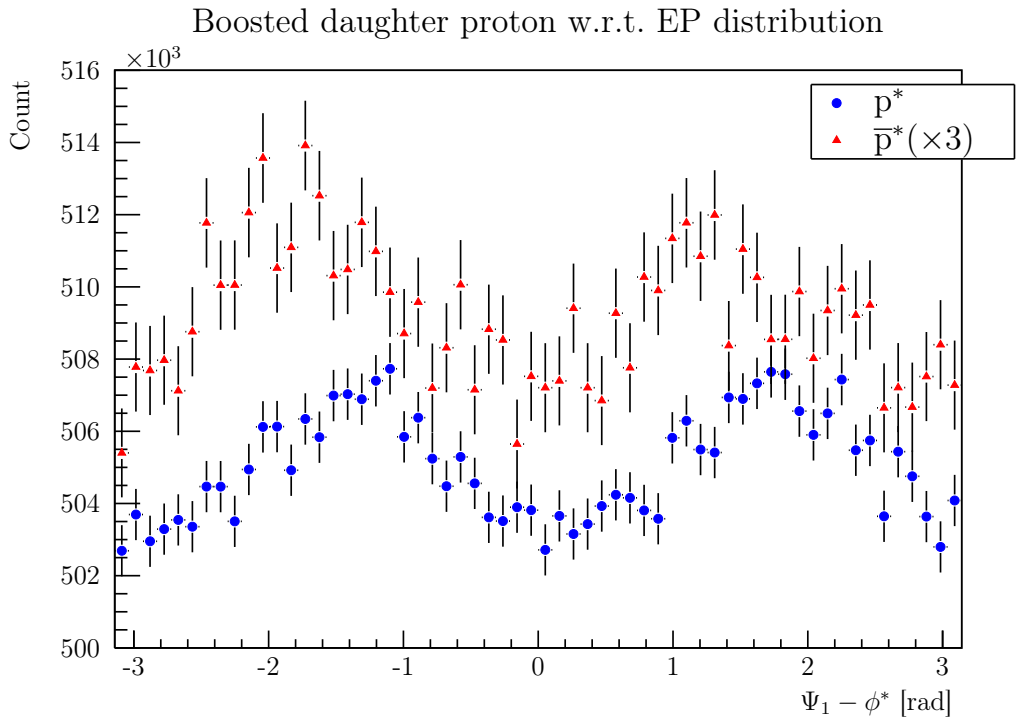

Figure 5.3: The angular distribution of daughter protons (p) and antiprotons ($\overline{p}$) in Λ ($\overline{\Lambda}$) rest frame ϕ^* with respect to the angle of EP Ψ_1 for Au-Au collisions at $\sqrt{s_{\rm NN}} = 27$ GeV.

5.2 Results of global Λ hyperon polarization

5.2.1 Invariant mass method

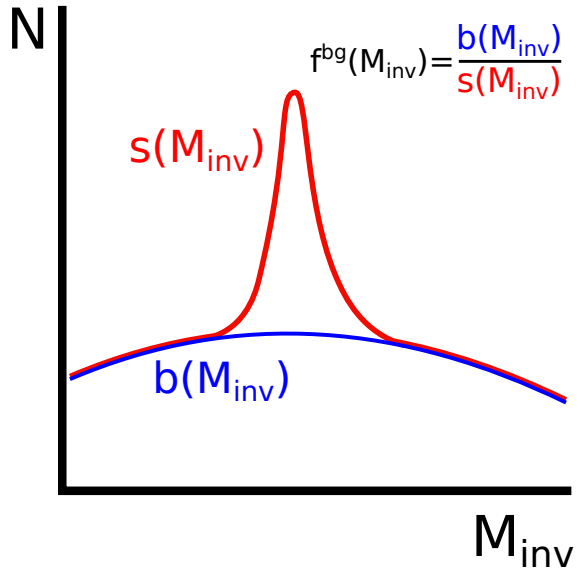

Figure 5.4: Schematic of the invariant mass of reconstructed candidates where $f^{Bg}(M_{inv})$ is a background fraction, $s(M_{inv}) = G(M_{inv})+\text{pol2}(M_{inv})$ is the measured signal and $b(M_{inv}) = \text{pol2}(M_{inv})$ is the background.

As was mentioned, the reconstruction of Λ hyperons has a residual background contamination. Some of the reconstructed Λs are not real Λs which influences the measured polarization, in particular the term $\langle\sin\big(\Psi_1 - \phi_p^*\big)\rangle$ in Eq. (1.5). The mean measured value of the sine term can be written as

$$\langle\sin\underbrace{(\Psi_1 - \phi_p^*)}_{\Delta\phi}\rangle = [1 - f^{Bg}(M_{inv})] \cdot \langle\sin(\Delta\phi)\rangle_{Sg} + f^{Bg}(M_{inv}) \cdot \langle\sin(\Delta\phi)\rangle_{Bg} \quad (5.4)$$

where $f^{Bg}(M_{inv})$ is the background fraction, see Fig. 5.4, $\langle\sin(\Delta\phi)\rangle_{Sg}$ is the polarization signal for (Λ) and $\langle\sin(\Delta\phi)\rangle_{Bg}$ is the polarization of the background [81].

The first step is to fit the invariant mass distribution for each centrality bin as was already described, see Fig. 3.5. The fit parameters $A_1, A_2, \sigma_1, \sigma_2, \mu_1, \mu_2, a, b$, and c were used to compute the $f^{Bg}(x)$ fraction as a function of the invariant mass.

Next, the $\langle\sin\big(\Psi_1 - \phi_p^*\big)\rangle$ was computed for each invariant mass bin and fitted with function in Eq. (5.4). An example of the fitted distribution for 30-50% centrality bins is shown in Fig. 5.5. The computed values of the polarization contributions of signal and background for Λ and $\overline{\Lambda}$ are gathered in Tab. 5.3.

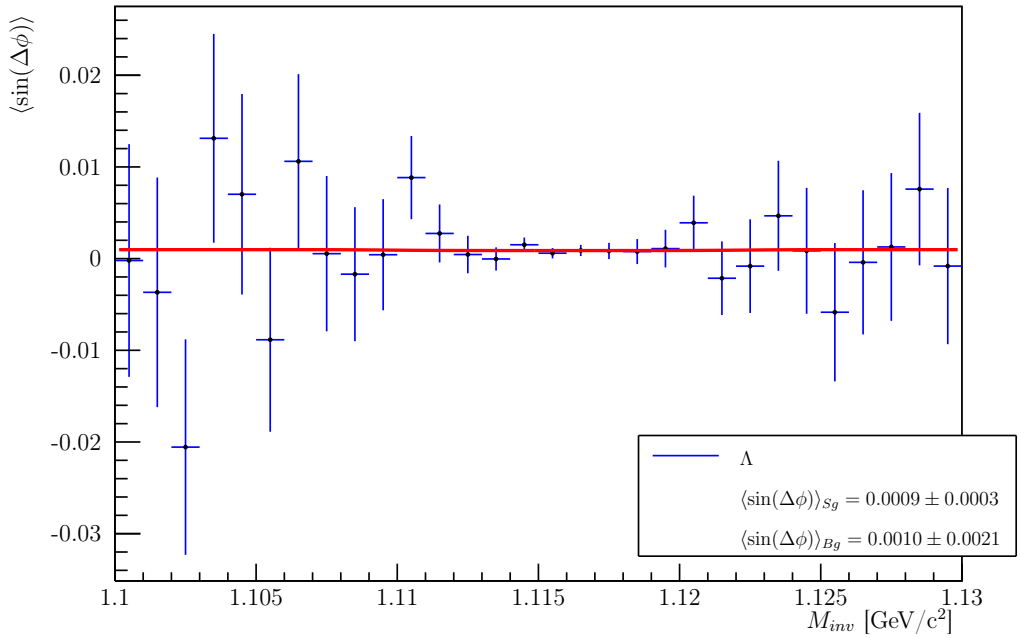

Figure 5.5: The measured $\langle \sin(\Delta\phi) \rangle$ as a function of on the invariant mass of Λ candidates in the centrality range 30-40%, fitted with the function in Eq. 5.4. See text for more details.

	$\langle \sin(\Delta\phi) \rangle_{\mathrm{Sg}}$ [10^{-4}]		$\langle \sin(\Delta\phi) \rangle_{\mathrm{Bg}}$ [10^{-4}]	
C [%]	Λ	$\overline{\Lambda}$	Λ	$\overline{\Lambda}$
80-70	3.87 ± 14.5	-10.2 ± 26.3	-58.3 ± 78.6	-134 ± 113
70-60	1.98 ± 8.98	0.8 ± 15.9	-13.0 ± 56.1	-53.4 ± 75.5
60-50	7.09 ± 6.09	-8.1 ± 10.8	-10.0 ± 41.5	7.4 ± 53.1
50-40	8.46 ± 4.25	-10.23 ± 7.63	16.8 ± 29.2	-36.0 ± 37.9
40-30	8.79 ± 3.14	-18.74 ± 5.74	9.8 ± 20.6	-14.9 ± 27.6
30-20	5.75 ± 2.43	-15.02 ± 4.53	15.5 ± 14.9	-16.3 ± 20.7
20-10	4.54 ± 1.96	-9.50 ± 3.71	3.6 ± 10.6	-23.0 ± 15.7
10-5	4.48 ± 1.79	-9.33 ± 3.41	8.08 ± 9.29	-23.8 ± 13.8
5-0	3.48 ± 1.60	-10.16 ± 3.10	3.69 ± 7.65	-18.8 ± 11.7

Table 5.3: The polarization contribution of the signal $\langle \sin(\Delta\phi) \rangle_{\mathrm{Sg}}$ and of the background $\langle \sin(\Delta\phi) \rangle_{\mathrm{Bg}}$ for Λ and $\overline{\Lambda}$ with $p_{\mathrm{T}} > 0.5$ GeV/c in Au-Au collision at $\sqrt{s_{\mathrm{NN}}} = 27$ GeV for each centrality range C.

The values of the global polarization of Λ and $\overline{\Lambda}$ as a function of centrality computed from Eq. (5.1) can be seen in Tab. 5.4. These results for Λ and $\overline{\Lambda}$ are consistent within uncertainty, cf. Fig. 5.6, however there is a hint of larger $\overline{\Lambda}$ polarization for centrality $C < 40\%$.

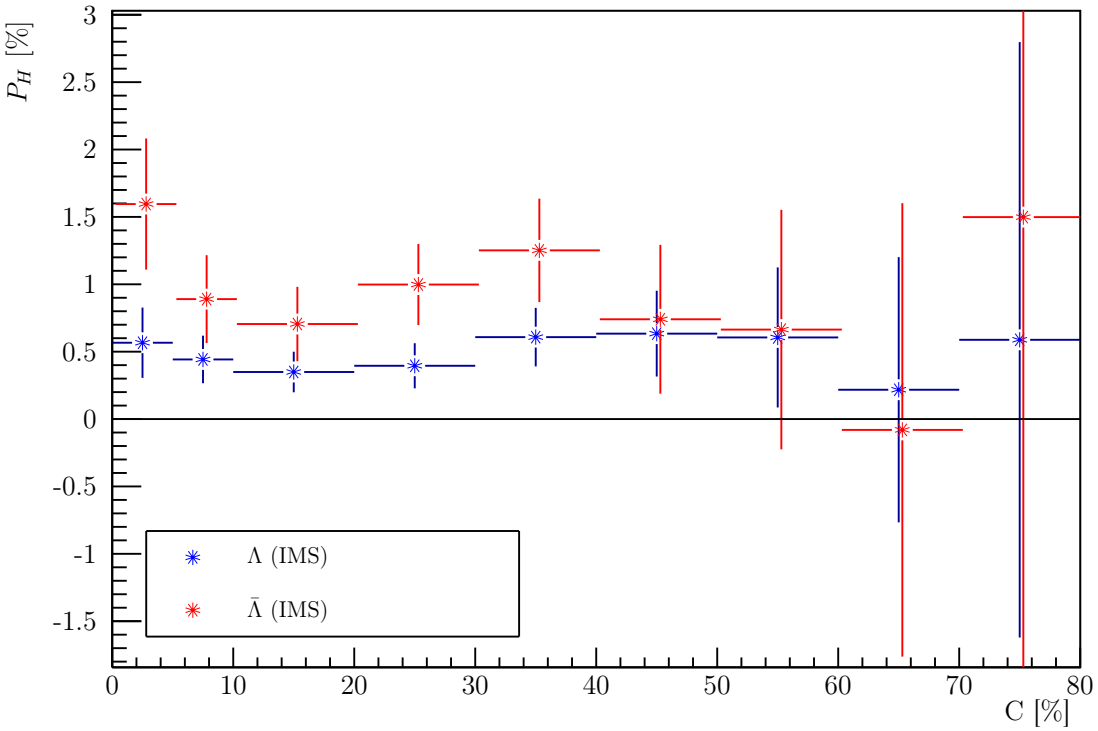

Figure 5.6: The global Λ and $\overline{\Lambda}$ hyperon polarization P_H as a function of centrality C for Au-Au collisions at $\sqrt{s_{\rm NN}} = 27$ GeV where the invariant mass method (IMM) is used. Results for $\overline{\Lambda}$ are slightly shifted to the right for clarity.

C [%]	P_Λ [%]	$P_{\overline{\Lambda}}$ [%]
80-70	0.59 ± 2.21	1.50 ± 3.86
70-60	0.217 ± 0.984	-0.08 ± 1.68
60-50	0.606 ± 0.520	0.664 ± 0.889
50-40	0.634 ± 0.318	0.740 ± 0.552
40-30	0.608 ± 0.217	1.252 ± 0.383
30-20	0.395 ± 0.167	0.998 ± 0.301
20-10	0.349 ± 0.151	0.705 ± 0.276
10-5	0.442 ± 0.176	0.890 ± 0.326
5-0	0.566 ± 0.261	1.595 ± 0.487

Table 5.4: The global Λ and $\overline{\Lambda}$ hyperon polarization P_Λ and $P_{\overline{\Lambda}}$ as a function of centrality C for Au-Au collisions at $\sqrt{s_{\rm NN}} = 27$ GeV where the invariant mass method (IMM) is used.

5.2.2 Event plane method

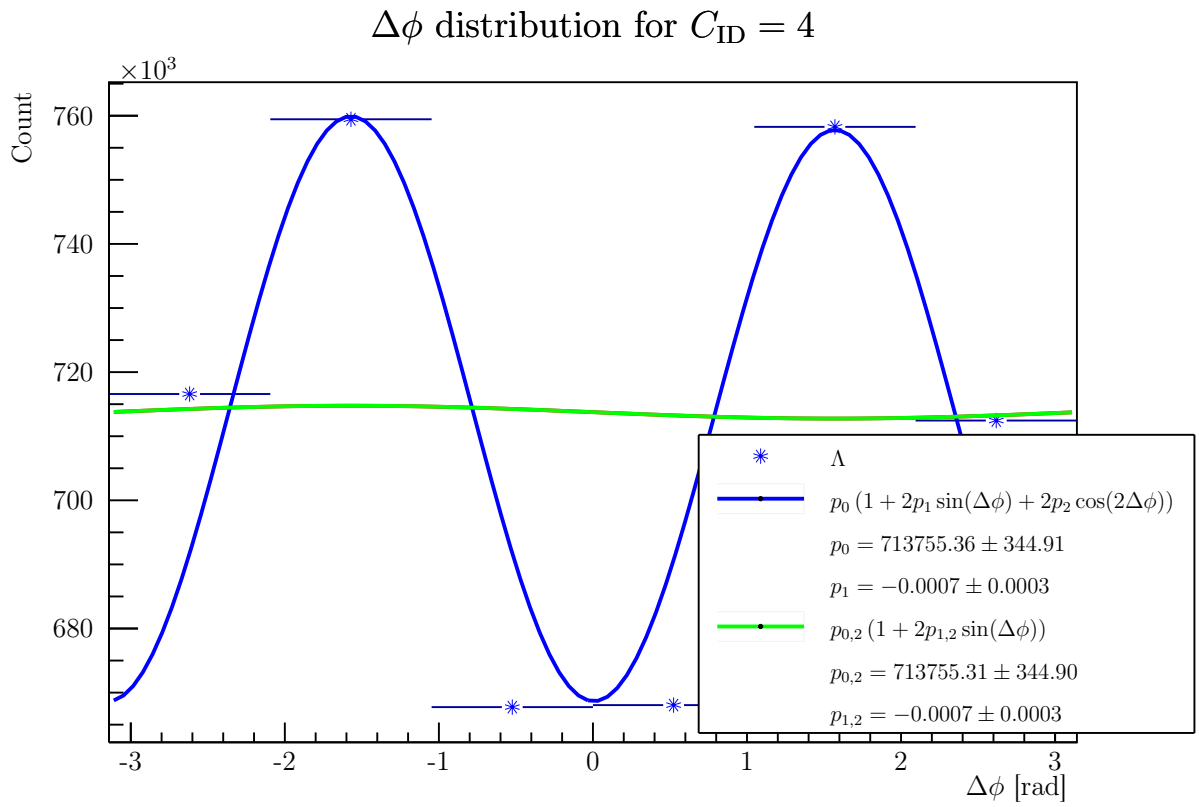

Figure 5.7: The measured signal yield S as a function of $\Delta\phi$ for Λ candidates in the centrality range 30-40%, fitted with the function in Eq. 5.5 where one considers first term of the sum (blue line) and without the sum terms (green line). See text for more details.

The event plane method is mainly used in flow analysis; however, it can be used for the polarization measurements as well. First, one counts the number of Λ and $\overline{\Lambda}$ (signal yield S) for each $\Delta\phi = \Psi_1 - \phi_p^*$ bin and for each centrality bin C. The width of the $\Delta\phi$ is chosen as $\pi/3$. Then the Λ yield is fitted by the function

$$p_0 \left[1 + 2p_1 \sin(\Delta\phi) + 2 \sum_{n=2}^{k} p_n cos(n\Delta\phi) \right] \tag{5.5}$$

where the value p_1 is the wanted $\langle \sin\left(\Psi_1 - \phi_p^*\right) \rangle$ value [10], [82]. An example can be seen in Fig. 5.7. The fit was done for two different versions of Eq. 5.5. First, just the first terms of the sum ($k = 2$) were considered. The related fitted values are labeled as p_n. In the second case, the sum in Eq. 5.5 is neglected and the related fitted values are labeled as $p_{n,2}$. The results show that one can consider just the first term with sinus in Eq. 5.5 for simplification, as the p_n values are the same in both cases. The second and higher order cosine terms p_n ($n \leq 2$) are related to the flow coefficient v_n. Hence, the fit with the cosine term describes the data better. However, the p_2

has a opposite sign contrary to expected elliptic flow v_2 which could be caused by the decay kinematics and STAR acceptance effects [82].

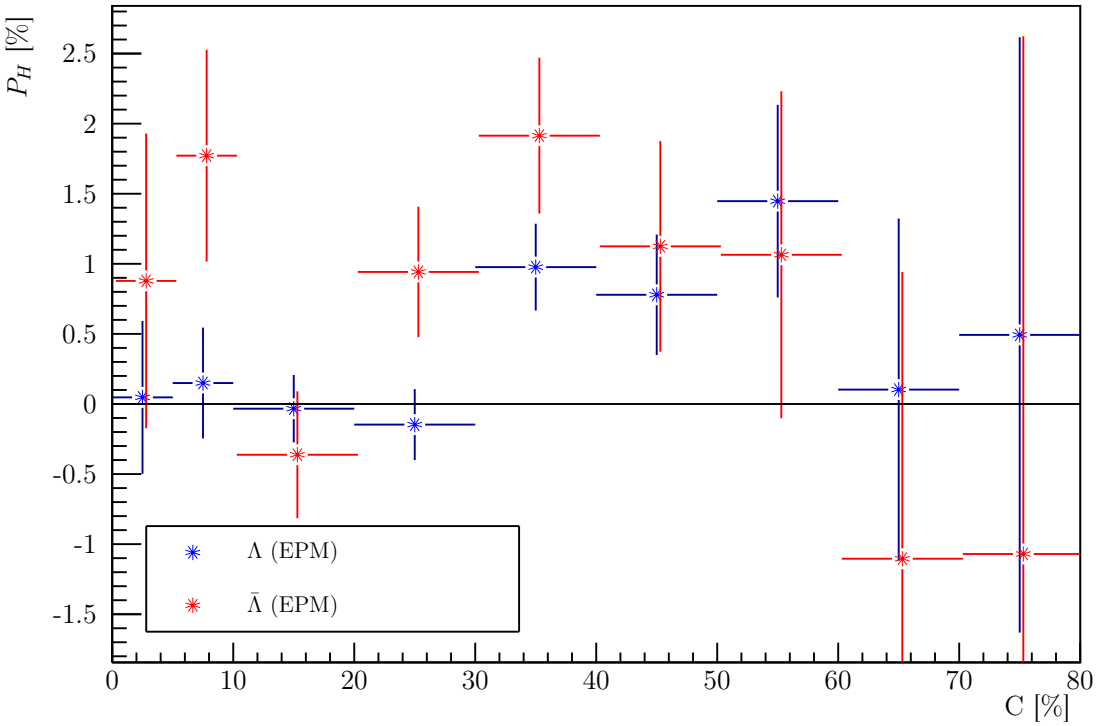

Figure 5.8: The global Λ and $\overline{\Lambda}$ hyperon polarization P_H as a function of centrality C for Au-Au collisions at $\sqrt{s_{\rm NN}} = 27$ GeV where the event plane method (EPM) is used. Results for $\overline{\Lambda}$ are slightly shifted to the right for clarity.

	Λ		$\overline{\Lambda}$	
C [%]	p_1 [10^{-4}]	$p_{1,2}$ [10^{-4}]	p_1 [10^{-4}]	$p_{1,2}$ [10^{-4}]
80-70	3.24 ± 14.0	3.47 ± 13.6	7.3 ± 25.1	7.0 ± 24.5
70-60	0.94 ± 11.14	1.3 ± 10.8	10.4 ± 19.3	10.0 ± 18.8
60-50	16.94 ± 8.05	16.41 ± 7.81	-12.9 ± 14.1	-12.2 ± 13.8
50-40	10.40 ± 5.73	9.94 ± 5.57	-15.5 ± 10.4	-15.3 ± 10.1
40-30	14.11 ± 4.48	13.65 ± 4.35	-28.65 ± 8.32	-28.19 ± 8.08
30-20	-2.14 ± 3.68	-2.16 ± 3.57	-14.18 ± 7.01	-13.69 ± 6.80
20-10	-0.44 ± 3.13	-0.46 ± 3.04	4.88 ± 6.09	4.76 ± 5.93
10-5	1.51 ± 4.00	1.28 ± 3.90	-18.56 ± 7.91	-17.30 ± 7.69
5-0	0.29 ± 3.35	0.34 ± 3.26	-5.59 ± 6.70	-5.94 ± 6.51

Table 5.5: The computed p_1, $p_{1,2}$ values of Λ and $\overline{\Lambda}$ hyperons for each centrality range C for Au-Au collisions at $\sqrt{s_{\rm NN}} = 27$ GeV. See text for more details.

C [%]	P_Λ [%]	$P_{\overline{\Lambda}}$ [%]
80-70	0.49 ± 2.12	-1.07 ± 3.69
70-60	0.10 ± 1.22	-1.10 ± 2.05
60-50	1.447 ± 0.687	1.06 ± 1.17
50-40	0.779 ± 0.430	1.125 ± 0.752
40-30	0.976 ± 0.310	1.914 ± 0.556
30-20	-0.147 ± 0.253	0.942 ± 0.466
20-10	-0.034 ± 0.241	-0.362 ± 0.453
10-5	0.150 ± 0.395	1.772 ± 0.755
5-0	0.047 ± 0.545	0.88 ± 1.05

Table 5.6: The global Λ and $\overline{\Lambda}$ hyperon polarization P_Λ and $P_{\overline{\Lambda}}$ for each centrality range C for Au-Au collisions at $\sqrt{s_{\rm NN}} = 27$ GeV where the invariant mass method (EPM) is used. See text for more details.

The p_1 and $p_{1,2}$ values are gathered in Tab. 5.5 and the final global polarization of Λ and $\overline{\Lambda}$ computed from Eq. (5.1) can be seen in Tab. 5.6 and Fig. 5.8.

In this case, the uncertainties of P_H for both hyperons are larger, but they are still consistent between each other within 2 sigma. For centralities $C < 50\%$, a hint of larger P_H for $\overline{\Lambda}$ than for Λ is there as well as in case of the IMM.

Chapter 6

Summary and disscusion

In this research task, the computation of global Λ polarization in Au-Au collisions at $\sqrt{s_{\mathrm{NN}}} = 27$ GeV from the STAR experiment at RHIC was the goal. The needed steps for this analysis included the reconstruction of the event plane of each collision, the reconstruction of the Λ and $\overline{\Lambda}$ hyperons, their daughter baryon angular distribution boosted to the rest frame of the mother particle with respect to the event plane, and two methods (namely the invariant mass method and event plane method) to extract the global Λ polarization P_H. The first estimation of the P_H was made for Λ and $\overline{\Lambda}$ using the above-mentioned methods that give reasonable and comparable results with the published ones in Nature [7].

The reconstructed event plane, especially its resolution is comparable with different results for the same dataset [80]. It should be also mentioned that the EPD results are at least 1.4 times better than when using BBC [80]. Thus the EPD was chosen in this work. The psi-shifting could be neglected as can be seen in Fig. 4.2 because the phi-weighting is a strong enough correction to flatten the Ψ_1 distribution, but this hypothesis should be tested, i.e. test it for different energy of collision and explore its impact on the resolution of the event plane. Therefore, one would have to introduce another correction or find a better set of parameters for ring-weighting instead of using eta-weighting. It could be concluded that the ideal number of iteration is 3 as can be seen in Fig. 4.5. The fourth and higher iterations does not significantly change the resolution. However, the interesting observation is that the second iteration slightly deteriorates the resolution. The ineffectiveness of the second iteration can be also seen in Fig. 4.3 where the Ψ_1 distribution is not flattened as much as just inverted. However, this effect can be also related to the fact that in the second iteration the Ring-weighting is used with parameters $(1, 1, 1, 1, \vec{0})$ including just the inner rings. If the weighting had been used from the beginning, this effect could have been avoided. Therefore, it is important to do at least 3 iterations.

The reconstructed Λ and $\overline{\Lambda}$ with $p_{\mathrm{T}} > 0.5$ GeV/c were considered in this work. This condition improves the statistical uncertainty of the global Λ polarization for the most central collisions although the target of interest is centrality range 20-50 %.

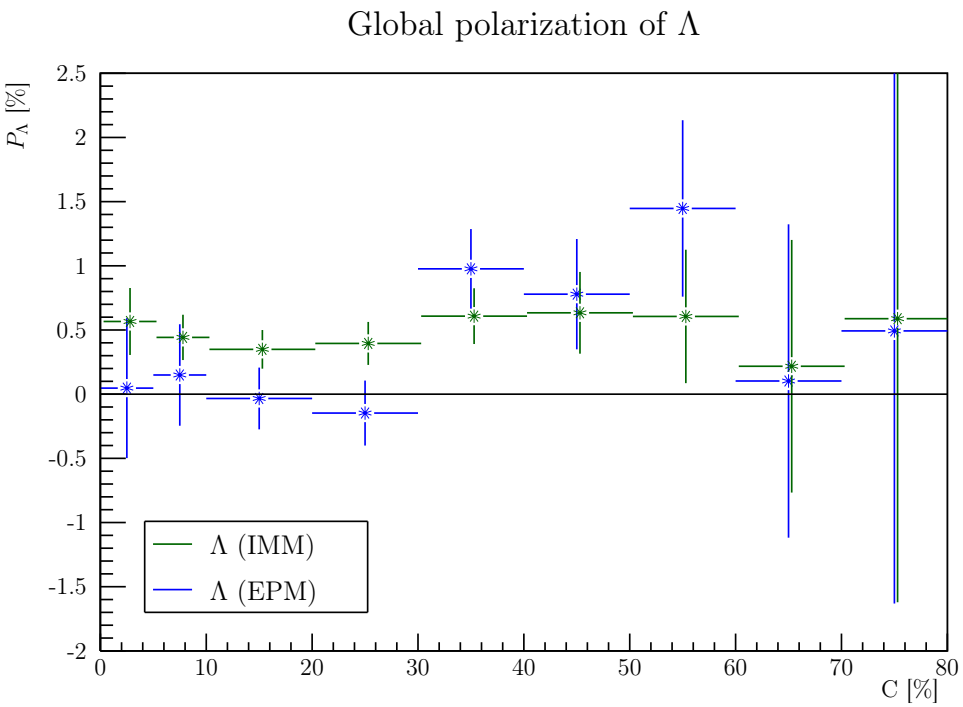

Figure 6.1: Comparison of the global Λ hyperon polarization P_Λ as a function of centrality C for Au-Au collisions at $\sqrt{s_{\mathrm{NN}}} = 27$ GeV where the invariant mass method (IMM) and the event plane method (EPM) are used. Results for IMM are slightly shifted to the right for clarity.

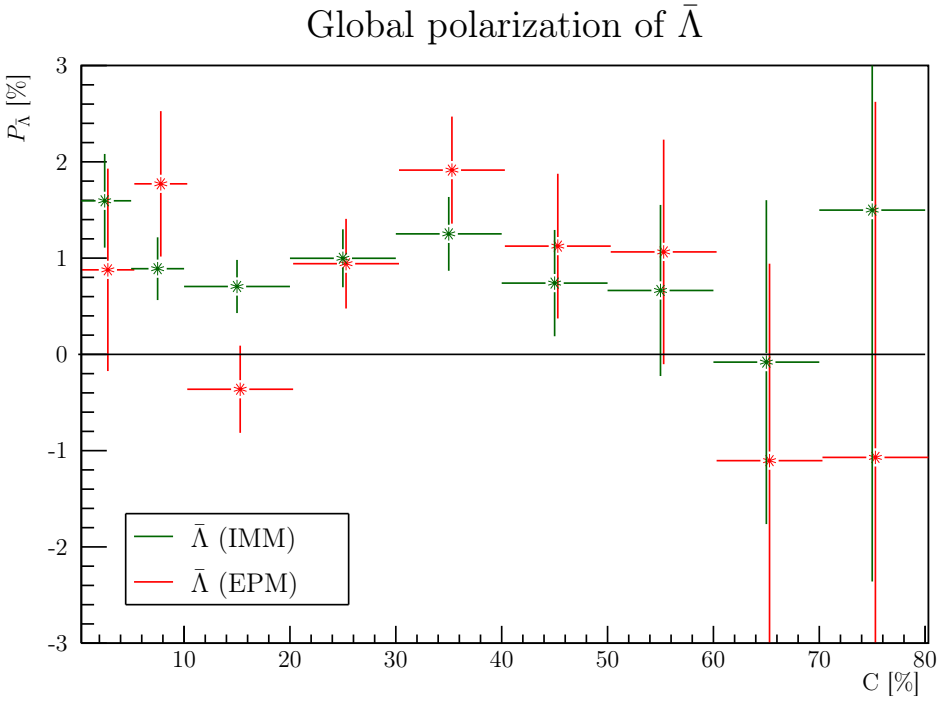

Figure 6.2: Comparison of the global $\overline{\Lambda}$ hyperon polarization $P_{\overline{\Lambda}}$ as a function of centrality C for Au-Au collisions at $\sqrt{s_{\mathrm{NN}}} = 27$ GeV where the invariant mass method (IMM) and the event plane method (EPM) are used. Results for EPM are slightly shifted to the right for clarity.

The invariant mass method and the event plane method which were used can be compared to each other for Λ and $\overline{\Lambda}$ in Fig. 6.1 and in Fig. 6.2, respectively. In the case of Λ, the both methods of computation of the global Λ polarization P_Λ are consistent within one sigma with each other except the centrality range 20-30 %. One can see that the polarization is weakest for the most central collisions (<20 %), strongest for the peripheral collisions (30-60 %), and most inaccurate for the most peripheral collisions (>60 %) which could be caused by lower statistics or by the larger fluctuation of the medium. This pattern is consistent with results shown in Fig. 1.6. For the $\overline{\Lambda}$, the methods are comparable within one sigma except the centrality range (10-20 %). Contrary to P_Λ, the polarization of the $\overline{\Lambda}$ is stronger in the centrality range and more variable for the most central collisions (<20 %).

The centrality range (20-50 %) can be compared with results introduced in Fig. 1.5. The non-central collisions, e.g. 20-50 %, are the most interesting because in the central collisions the strong vorticity is not expected due to symmetry of the system and in the peripheral collisions, the medium with the vorticity is smaller or do not have to be created. The computed Λ ($\overline{\Lambda}$) hyperon global polarization in centrality range 20-50 % is gathered in Tab. 6.1. The P_Λ is in agreement with the official result published in Nature within the uncertainties except for the centrality range 20-30 % for both methods. Notice, it is the same centrality range being not in accordance for the different methods IMM and EPM. In the case of $P_{\overline{\Lambda}}$, all values are consistent with the published data for both methods.

	C [%]	20-30	30-40	40-50	20-50 (Nature 548.62 [7])
P_Λ [%]	IMM	0.395 ± 0.167	0.608 ± 0.217	0.634 ± 0.318	1.047 ± 0.282
	EPM	-0.147 ± 0.253	0.976 ± 0.310	0.779 ± 0.430	
$P_{\overline{\Lambda}}$ [%]	IMM	0.998 ± 0.301	1.252 ± 0.383	0.740 ± 0.552	1.245 ± 0.471
	EPM	0.942 ± 0.466	1.914 ± 0.556	1.125 ± 0.752	

Table 6.1: The global Λ and $\overline{\Lambda}$ hyperon polarization P_Λ and $P_{\overline{\Lambda}}$ as a function of centrality C for Au-Au collisions at $\sqrt{s_{\rm NN}}$ = 27 GeV where the invariant mass method (IMM) and the event plane method (EPM).

The comparison of the invariant mass method and the event plane method is important tool to crosscheck the obtained results, and can be used to determine the systematic uncertainty of the polarization.

The presented P_H results are the first look. They are extremely very reasonable and in agreement with the published values, however, need further refinement and corrections, e.q. acceptance or helicity correction. The first one is related to the acceptance of the detector and the second one to the fact that some Λ and $\overline{\Lambda}$ are easier to reconstruct than others. The refined results are the last step to compute the initial vorticity of the QGP and this will be part of my following work.

The published results in Nature [7] were done using older data. The repeating of the measurement using the newer dataset is important to confirm the previous results or get more precise results due to larger statistics in more centrality ranges.

Conclusion

In this thesis the global Λ ($\overline{\Lambda}$) hyperon polarization in Au-Au collisions at energy $\sqrt{s_{\mathrm{NN}}}$ = 27 GeV from the STAR experiment was computed. For this purpose, the event plane of collisions was reconstructed using information from the event plane detector. To refine the angle of EP, the phi-weighting, eta-weighting, recentering, and psi-shifting corrections were used. The resolution of the EP was successfully estimated by the sub-event method. The Λ ($\overline{\Lambda}$) candidates were reconstructed via the Kalman filter using the topological selection criteria. The daughter baryon angular distribution was boosted to the rest frame of their mother particle Λ ($\overline{\Lambda}$) with respect to the related event plane.

The global polarization P_{Λ} and $P_{\overline{\Lambda}}$ were successfully extracted from data contaminated by background by using two different methods: the invariant mass method and the event plane method. The result polarization, see Tab. 6.1, are consistent within two sigma with the official results published in Nature [7] for centrality range 20-50 %. Both methods give consistent results within one sigma except the centrality range C = 20-30 % for Λ hyperon and C = 10-20 % for $\overline{\Lambda}$ which are consistent within two sigma.

The next step that will be included in my following work is to refine the results by using acceptance and helicity correction, to compute the related vorticity of the QGP, to estimate systematic uncertainties, and to compare the polarization with the simulated results from hydro model.

Bibliography

[1] PASECHNIK, R., & ŠUMBERA, M. (2017). Phenomenological Review on Quark–Gluon Plasma: Concepts vs. Observations. Universe, 3(1), 7. https://doi.org/10.3390/universe3010007

[2] SHI, S. (2019). Soft and Hard Probes of QCD Topological Structures in Relativistic Heavy-Ion Collisions (Springer Theses) (1st ed. 2019 ed.). Springer.

[3] TSERRUYA, I. (2010). Electromagnetic Probes. Relativistic Heavy Ion Physics, 176–207. https://doi.org/10.1007/978-3-642-01539-7_7

[4] SATZ, H. (2018). Extreme States of Matter in Strong Interaction Physics: An Introduction (Lecture Notes in Physics Book 945) (2nd ed.) [E-book]. Springer.

[5] CIFARELLI, L., CSERNAI, L., & STÖCKER, H. (2012). The Quark-Gluon Plasma, a nearly perfect fluid. Europhysics News, 43(2), 29–31. https://doi.org/10.1051/epn/2012206

[6] CHEN, C. H. (2014). Studying the Early Universe via Quark-Gluon Plasma. Nuclear Physics B - Proceedings Supplements, 246–247, 38–41. https://doi.org/10.1016/j.nuclphysbps.2013.10.063

[7] Global Λ hyperon polarization in nuclear collisions. (2017). Nature, 548(7665), 62–65. https://doi.org/10.1038/nature23004

[8] BECATTINI, F., & LISA, M. A. (2020). Polarization and Vorticity in the Quark–Gluon Plasma. Annual Review of Nuclear and Particle Science, 70(1), 395–423. https://doi.org/10.1146/annurev-nucl-021920-095245

[9] KISEL, I. (2020). Real-Time Event Reconstruction and Analysis in CBM and STAR Experiments. Journal of Physics: Conference Series, 1602, 012006. https://doi.org/10.1088/1742-6596/1602/1/012006

[10] ADAM, J., et al. (2018). Global polarization of Λ hyperons in Au + Au collisions at $\sqrt{s_{\mathrm{NN}}} = 200$ GeV. Physical Review C, 98(1). https://doi.org/10.1103/physrevc.98.014910

[11] Quark-matter fireballs hashed out in Protvino. (2021, February 12). CERN Courier. https://cerncourier.com/a/quark-matter-fireballs-hashed-out-in-protvino/

[12] HEINZ, U., & JACOB, M. (2000). Evidence for a New State of Matter: An Assessment of the Results from the CERN Lead Beam Programme. https://arxiv.org/pdf/nucl-th/0002042.pdf

[13] RAFELSKI, J. (2020). Discovery of Quark-Gluon Plasma: Strangeness Diaries. The European Physical Journal Special Topics, 229(1), 1–140. https://doi.org/10.1140/epjst/e2019-900263-x

[14] ADCOX, K., et. al. (2005). Formation of dense partonic matter in relativistic nucleus–nucleus collisions at RHIC: Experimental evaluation by the PHENIX Collaboration. Nuclear Physics A, 757(1–2), 184–283. https://doi.org/10.1016/j.nuclphysa.2005.03.086

[15] BAZAVOV, A., et. al. (2019). Chiral crossover in QCD at zero and non-zero chemical potentials. Physics Letters B, 795, 15–21. https://doi.org/10.1016/j.physletb.2019.05.013

[16] GYULASSY, M. (2004). The QGP Discovered at RHIC. Invited Talk at NATO Advanced Study Institute: Structure and Dynamics of Elementary Matter. Published. https://arxiv.org/pdf/nucl-th/0403032.pdf

[17] K. YAGI, T. HATSUDA, and Y. MIAKE, "Quark-gluon plasma: From big bang to little bang," Camb. Monogr. Part. Phys. Nucl. Phys. Cosmol. 23, 1–446 (2005).

[18] KRAMER, M., & SOLER, F. (2019). Large Hadron Collider Phenomenology (1st ed.). CRC Press.

[19] ANDRONIC, A., BRAUN-MUNZINGER, P., & STACHEL, J. (2009). Thermal hadron production in relativistic nuclear collisions: The hadron mass spectrum, the horn, and the QCD phase transition. Physics Letters B, 673(2), 142–145. https://doi.org/10.1016/j.physletb.2009.02.014

[20] NOUICER, R. (2016). New state of nuclear matter: Nearly perfect fluid of quarks and gluons in heavy-ion collisions at RHIC energies. The European Physical Journal Plus, 131(3). https://doi.org/10.1140/epjp/i2016-16070-2

[21] S. BEOLE, Looking for Quark Gluon Plasma in Pb–Pb Collisions at 158 GeVrc, Universita Degli Studi Di Torino, Ph.D. Thesis, 1998.

[22] SEKIHATA, D. (2019). Energy and system dependence of nuclear modification factors of inclusive charged particles and identified light hadrons measured in p–Pb, Xe–Xe and Pb–Pb collisions with ALICE. Nuclear Physics A, 982, 567–570. https://doi.org/10.1016/j.nuclphysa.2018.10.052

[23] DE GODOY, D. M. (2013). Measurements of the nuclear modification factor and the elliptic azimuthal anisotropy of heavy flavours with ALICE. Journal of Physics: Conference Series, 458, 012013. https://doi.org/10.1088/1742-6596/458/1/012013

[24] TALLEY, L. D. (2011). Descriptive Physical Oceanography: An Introduction (6th ed.). Academic Press.

[25] ZYLA, P. A., et. al. (2021). pdgLive. Particle Data Group. https://pdg.lbl.gov/2021/listings/contents_listings.html

[26] ADAM, J., et al. (2021). Global Polarization of Ξ and Ω Hyperons in Au+Au Collisions at $\sqrt{s_{\mathrm{NN}}}$=200 GeV. Physical Review Letters, 126(16). https://doi.org/10.1103/physrevlett.126.162301

[27] AGS Booster Celebrates a Quarter-Century of Service. (2016, June 27). Brookhaven National Laboratory. https://www.bnl.gov/newsroom/news.php?a=26425

[28] SHILTSEV, V., & ZIMMERMANN, F. (2021). Modern and future colliders. Reviews of Modern Physics, 93(1). https://doi.org/10.1103/revmodphys.93.015006

[29] FRASER, G. (1997). The Quark Machines: How Europe Fought the Particle Physics War, Second Edition (2nd ed.). CRC Press.

[30] BAYM, G. (2002). RHIC: From dreams to beams in two decades. Nuclear Physics A, 698(1–4), xxiii–xxxii. https://doi.org/10.1016/s0375-9474(01)01342-2

[31] LITVINENKO, V. N., et al. (2008). Experience with IBS-suppression lattice in RHIC. 1th Biennial European Particle Accelerator Conference (EPAC 2008). Published. https://www.bnl.gov/isd/documents/43238.pdf

[32] TANNENBAUM, M. J. (2019). Latest Results from RHIC + Progress on Determining q $\hat{\mathrm{L}}$ in RHI Collisions Using Di-Hadron Correlations. Universe, 5(6), 140. https://doi.org/10.3390/universe5060140

[33] NAGLE, J. L., & ULLRICH, T. S. (2001). Heavy Ion Experiments at RHIC: The First Year. QCD Perspectives on Hot and Dense Matter. Published. https://arxiv.org/abs/nucl-ex/0203007v1

[34] MONTAG, C. (2019). RHIC status and plans. 25th international conference on the application of accelerators in research and industry. Published. https://doi.org/10.1063/1.5127686

[35] RHIC Run Overview. (2021, June 8). Run Overview of the Relativistic Heavy Ion Collider. https://www.rhichome.bnl.gov/RHIC/Runs/

[36] GORBUNOV, Y., CHERNEY, M., FUJITA, J., & WAGGONER, W. (2007). Slow control system for the STAR experiment. 2007 IEEE Nuclear Science Symposium Conference Record. Published. https://doi.org/10.1109/nssmic.2007.4436465

[37] YANG, Q. (2019). The STAR BES-II and Forward Rapidity Physics and Upgrades. Nuclear Physics A, 982, 951–954. https://doi.org/10.1016/j.nuclphysa.2018.10.029

[38] LIU, C., et. al. (2019). Fixed Target Operation at RHIC in 2019. JACoW Publishing, 3. https://doi.org/10.18429/JACoW-NAPAC2019-TUPLO05

[39] CAINES, H. (2020). STAR Status of Beam Energy Scan, BUR for Runs 21 and 22. BNL NPP 2020 PAC Meeting. Published. https://indico.bnl.gov/event/7881/contributions/40773/attachments/30329/47476/BUR-2020-PAC.pdf

[40] RADHAKRISHNAN, S. (2021). Updates on Flavor Production from STAR. The 19th International Conference on Strangeness in Quark Matter (SQM 2021). Published. https://drupal.star.bnl.gov/STAR/files/FlavorProductionSTAR_SQM2021_v3d.pdf

[41] MEEHAN, K. C. (2016). The fixed-target experiment at STAR. Journal of Physics: Conference Series, 742, 012022. https://doi.org/10.1088/1742-6596/742/1/012022

[42] YE, Z. (2019). Open Heavy Flavor from STAR [Slides]. Moriond. http://moriond.in2p3.fr/QCD/2019/FridayMorning/Ye.pdf

[43] ANDERSON, M., et. al. (2003). The STAR time projection chamber: a unique tool for studying high multiplicity events at RHIC. Nuclear Instruments and Methods in Physics Research Section A: Accelerators, Spectrometers, Detectors and Associated Equipment, 499(2–3), 659–678. https://doi.org/10.1016/s0168-9002(02)01964-2

[44] The STAR TOF Collaboration. (2004). Proposal for a Large Area Time of Flight System for STAR. The STAR experiment. https://www.star.bnl.gov/public/tof/publications/TOF_20040524.pdf

[45] SHAO, M., BARANNIKOVA, O., DONG, X., FISYAK, Y., RUAN, L., SORENSEN, P., & XU, Z. (2006). Extensive particle identification with TPC and TOF at the STAR experiment. Nuclear Instruments and Methods in Physics Research Section A: Accelerators, Spectrometers, Detectors and Associated Equipment, 558(2), 419–429. https://doi.org/10.1016/j.nima.2005.11.251

[46] BEDDO, M., et al. (2003). The STAR Barrel Electromagnetic Calorimeter. Nuclear Instruments and Methods in Physics Research Section A: Accelerators, Spectrometers, Detectors and Associated Equipment, 499(2–3), 725–739. https://doi.org/10.1016/s0168-9002(02)01970-8

[47] The STAR Collaboration. (1992). Conceptual Design Report. https://drupal.star.bnl.gov/STAR/files/StarCDR.pdf

[48] WHITTEN, C. A., KPONOU, A., MAKDISI, Y., & ZELENSKI, A. (2008). The Beam-Beam Counter: A Local Polarimeter at STAR. AIP Conference Proceedings. Published. https://doi.org/10.1063/1.2888113

[49] LLOPE, W., et. al. (2014). The STAR Vertex Position Detector. Nuclear Instruments and Methods in Physics Research Section A: Accelerators, Spectrometers, Detectors and Associated Equipment, 759, 23–28. https://doi.org/10.1016/j.nima.2014.04.080

[50] JUDD, E., BLAND, L., CRAWFORD, H., ENGELAGE, J., LANDGRAF, J., LLOPE, W., NELSON, J., NG, M., OGAWA, A., PERKINS, C., VISSER, G., & XU, Z. (2018). The evolution of the STAR Trigger System. Nuclear Instruments and Methods in Physics Research Section A: Accelerators, Spectrometers, Detectors and Associated Equipment, 902, 228–237. https://doi.org/10.1016/j.nima.2018.03.070

[51] YANG, C., & YANG, Q. (2020). The STAR Detector Upgrades for the BES-II and at Forward Rapidity. Journal of Instrumentation, 15(07), C07040. https://doi.org/10.1088/1748-0221/15/07/c07040

[52] MEEHAN, K. (2017). STAR Results from Au+Au Fixed-Target Collisions at $\sqrt{s_{\mathrm{NN}}} = 4.5$ GeV. Nuclear Physics A, 967, 808–811. https://doi.org/10.1016/j.nuclphysa.2017.06.007

[53] The STAR Collaboration. (2020). The STAR Beam Use Request for Run-21, Run-22 and data taking in 2023–25. https://drupal.star.bnl.gov/STAR/system/files/userfiles/5051/STAR%20BUR%20Runs%2021-25%20v2.pdflabel

[54] ADAMS, J., et. al. (2020). The STAR event plane detector. Nuclear Instruments and Methods in Physics Research Section A: Accelerators, Spectrometers, Detectors and Associated Equipment, 968, 163970. https://doi.org/10.1016/j.nima.2020.163970

[55] COOPER, D. (2020, September 22). The Next U.S. Particle Accelerator Will Be Built On Long Island By 2031. Entrepreneur. https://www.entrepreneur.com/article/356548

[56] Science Requirements and Detector Concepts for the Electron-Ion Collider: EIC Yellow Report (BNL-220990-2021-FORE). (2021). https://arxiv.org/abs/2103.05419

[57] U.S. Department of Energy Selects Brookhaven National Laboratory to Host Major New Nuclear Physics Facility. (2020, January 9). Brookhaven National Laboratory. https://www.bnl.gov/newsroom/news.php?a=116996

[58] Production picoDst Size on DD. (2021, July 2). The STAR Experiment. https://www.star.bnl.gov/public/comp/prod/localdata/DDpicosize.html

[59] PRUNEAU, C. A. (2017). Data Analysis Techniques for Physical Scientists (1st ed.). Cambridge University Press.

[60] GORBUNOV, S. (2013, March). On-line reconstruction algorithms for the CBM and ALICE experiments (No. 319912507). Universitätsbibliothek Johann Christian Senckenberg. https://d-nb.info/1043977902/34

[61] FRUHWIRTH, R. (2000). Data Analysis Techniques for High-Energy Physics (Cambridge Monographs on Particle Physics, Nuclear Physics and Cosmology) (2nd ed.). Cambridge University Press.

[62] ZYZAK, M., KISEL, I., KULAKOV, I., & VASSILIEV, I. (2012). The KF Particle Finder package for short-lived particles reconstruction for CBM (PHN-NQM-EXP-50). http://repository.gsi.de/record/51984/files/PHN-NQM-EXP-50.pdf

[63] ZYZAK, M. (2018, December 11). KFParticle tutorial [Slides]. The STAR Experiment. https://drupal.star.bnl.gov/STAR/system/files/KFParticleTutorial_11.12.2018.pdf

[64] BRUN, R., & RADEMAKERS, F. (1997). ROOT — An object oriented data analysis framework. Nuclear Instruments and Methods in Physics Research Section A: Accelerators, Spectrometers, Detectors and Associated Equipment, 389(1–2), 81–86. https://doi.org/10.1016/s0168-9002(97)00048-x

[65] GRIFFITHS, D. J. (1987). Introduction to Elementary Particles. Wiley.

[66] SHARMA, S. K. (2008). Atomic And Nuclear Physics. Pearson Education.

[67] GAL, A. (2020). Recent progress on hypernuclei. Journal of Physics: Conference Series, 1643, 012170. https://doi.org/10.1088/1742-6596/1643/1/012170

[68] ZYZAK, M. (2017). Online selection of short-lived particles on many-core computer architectures in the CBM experiment at FAIR (No. 385874006). Universitätsbibliothek Johann Christian Senckenberg. http://publikationen.ub.uni-frankfurt.de/frontdoor/index/index/year/2016/docId/41428

[69] CHATRCHYAN, S., et. al. (2013). Measurement of the elliptic anisotropy of charged particles produced in PbPb collisions at $\sqrt{s_{\mathrm{NN}}}$=2.76TeV. Physical Review C, 87(1). https://doi.org/10.1103/physrevc.87.014902

[70] IVASHKIN, A., FINOGEEV, D., GOLUBEVA, M., GUBER, F., IZVESTNYY, A., MOROZOV, S., & STRIZHAK, A. (2019). Determination of geometry of heavy ion collisions with forward hadron calorimeter (FHCal) at MPD/NICA. EPJ Web of Conferences, 204, 07002. https://doi.org/10.1051/epjconf/201920407002

[71] POSKANZER, A. M., & VOLOSHIN, S. A. (1998). Methods for analyzing anisotropic flow in relativistic nuclear collisions. Physical Review C, 58(3), 1671–1678. https://doi.org/10.1103/physrevc.58.1671

[72] LISA, M. (2017, October 12). EPD calibration for Au+Au 2017 (and method in general) | The STAR experiment. The STAR Experiment. https://drupal.star.bnl.gov/STAR/blog/lisa/epd-calibration-auau-2017-and-method-general

[73] VOLOSHIN, S. A., POSKANZER, A. M., & SNELLINGS, R. (2010). Collective Phenomena in Non-Central Nuclear Collisions. Relativistic Heavy Ion Physics, 293–333. https://doi.org/10.1007/978-3-642-01539-7_10

[74] LISA, M. (2018, June 13). Phi-weighting and optimizing ring weights in Au+Au 27 GeV | The STAR experiment. The STAR Experiment. https://drupal.star.bnl.gov/STAR/blog/lisa/phi-weighting-and-optimizing-ring-weights-auau-27-gev

[75] LISA, M. (2018, May 30). EP resolution and the eta dependence of directed flow in Au+Au collisions | The STAR experiment. The STAR Experiment. https://drupal.star.bnl.gov/STAR/blog/lisa/ep-resolution-and-eta-dependence-directed-flow-auau-collisions

[76] JAMES, F. (1994). MINUIT Function Minimization and Error Analysis: Reference Manual Version 94.1 (CERN-D-506). https://inspirehep.net/literature/1258343

[77] LISA, M. (2018b, October 24). Optimizing EP[1] resolution in Au27Au: From ring-dependent weights to eta-dependent weights | The STAR experiment. The STAR Experiment. https://drupal.star.bnl.gov/STAR/blog/lisa/optimizing-ep1-resolution-au27au-ring-dependent-weights-eta-dependent-weights

[78] BARRETTE, J., et. al. (1997). Proton and pion production relative to the reaction plane in Au + Au collisions at 11AGeV/c. Physical Review C, 56(6), 3254–3264. https://doi.org/10.1103/physrevc.56.3254

[79] POSKANZER, A. M., & VOLOSHIN, S. A. (1998b). Methods for analyzing anisotropic flow in relativistic nuclear collisions. Physical Review C, 58(3), 1671–1678. https://doi.org/10.1103/physrevc.58.1671

[80] UPSAL, I. (2019, October 11). Determining eta weights for EPD event plane analysis | The STAR experiment. The STAR Experiment. https://drupal2.star.bnl.gov/STAR/blog/iupsal/determining-eta-weights-epd-event-plane-analysis

[81] UPSAL, I. (2018). GLOBAL POLARIZATION OF THE $\Lambda/\overline{\Lambda}$ STAR BES. Ohio State University. https://drupal.star.bnl.gov/STAR/files/UpsalThesisV4.pdf

[82] NIIDA, T., & VOLOSHIN, A. (2018, April). Global polarization of Λ hyperons in Au+Au collisions at $\sqrt{s_{\mathrm{NN}}} = 200$ GeV.